Fast neutral-atom transport and transfer between optical tweezers

Cristina Cicali,[1,2,*] Martino Calzavara,[1,2] Eloisa Cuestas,[1,3] Tommaso Calarco,[1,2,4] Robert Zeier,[1] and Felix Motzoi[1,2,†]

[1] *Forschungszentrum Jülich GmbH, Peter Grünberg Institute, Quantum Control (PGI-8), 52425 Jülich, Germany*
[2] *Institute for Theoretical Physics, University of Cologne, Zülpicher Straße 77, 50937 Cologne, Germany*
[3] *Quantum Systems Unit, Okinawa Institute of Science and Technology Graduate University, Onna, Okinawa 904-0495, Japan*
[4] *Dipartimento di Fisica e Astronomia, Università di Bologna, 40127 Bologna, Italy*

(Received 24 January 2025; revised 28 May 2025; accepted 14 July 2025; published 28 August 2025)

We study the optimization of the transport and transfer of neutral atoms between optical tweezers, both critical steps in the implementation of quantum computers and simulators. We analyze four experimentally relevant pulse shapes (piecewise linear, piecewise quadratic, minimum jerk, and a combination of linear and minimum jerk), and we also develop a protocol using shortcuts-to-adiabaticity (STA) methods to crucially incorporate the time-dependent effects of static traps. By computing a measure of the final transport error and two measures of the heating during transport, we show that our proposed STA protocol comprehensively outperforms all the experimentally inspired pulses. After further optimizing the pulse shapes, we find a lower bound on the protocol duration, compatible with the time at which the vibrational excitations exceed half of the states hosted by the moving tweezer. This lower bound is at least eight times faster than the one reported in recent experiments, which highlights the importance of including and optimizing the transfer from and to static traps, which may be the largest bottleneck to speed. Finally, our STA results demonstrate that a modulation in the depth of the moving tweezer designed to time-dependently counteract the effect of the static traps is key to reducing errors and reducing the pulse duration. To motivate the implementation of our STA pulses in future experiments, we provide a simple analytical approximation for the moving-tweezer position and depth controls.

DOI: 10.1103/7r3w-8m61

I. INTRODUCTION

Over the last decade we have witnessed a sustained growth in the capabilities for quantum information processing and simulation, based on significant progress in both the confinement and control of atomic arrays [1–7], with a critical role played by the precise manipulation and transport of neutral atoms in optical tweezers [8,9]. In state-of-the-art experiments, the atoms are usually cooled to a temperature of 10–100 μK and then stochastically loaded (with a probability of about 0.5, or half-filling) from a magneto-optical trap into a set of space- and time-controlled Gaussian traps or optical lattices. In general, the experimental setup involves a spatial light modulator to create the static trap array, while the moving optical tweezers are controlled by acousto-optic deflectors (AODs) [1,6,8]; other approaches for similar experiments rely only on tweezers generated and controlled via AODs [9–12]. These tweezers allow for a precise rearrangement of stochastically loaded atoms, enable nonlocal connectivity, and eliminate the need to prepare a new ensemble of atoms after each measurement, thus enhancing experimental efficiency [13].

The basic requirements for a quantum processor include initialization and storage of qubits in a quantum register, bringing qubits sufficiently close to realize quantum gates and the final readout [14]. Therefore, efficient atom transport is not only a key step in performing controlled translations from the preparation or cooling chamber to the science cell but also allows for on-demand interactions to realize quantum operations in the correct location (including both processing and storing sites) and with precise timing. In this context, fast and accurate manipulation of atomic motion emerges as a central requirement for quantum technologies to preserve coherence while attaining high fidelities between the final state and a predefined

*Contact author: c.cicali@fz-juelich.de
†Contact author: f.motzoi@fz-juelich.de

target state [15]. Moreover, atom transport appears as a potential long-term bottleneck in quantum computing with cold atoms, given that other operations are expected to be significantly faster [16].

Several experiments have been undertaken to study atom shuttling [17–20], where the ideal goal is to obtain a final state as close as possible to the initial state while avoiding losses and vibrational excitations. Although the use of long transport times (adiabatic processes) may seem the natural path to high final fidelities, they also translate into the accumulation of decoherence and experimental noise [18]. Conversely, diabatic (i.e., fast) processes lead by default to higher excitations and thus to overheating and losses. It is therefore necessary to find a trade-off between high fidelity and transport time [6,7]. In this work, we focus on the optimization of the transport and transfer of atoms between optical tweezers to speed up these operations while avoiding unwanted excitations. In particular, the protocols we design include the capturing and releasing of the atom from and to static traps (which we refer to as *transfer*) as well as the *transport* itself. At the end of the process, the atom is located in the desired position. This results in increased flexibility in experimental operations (once the protocol is completed, the moving tweezers are free to be used for other tasks) and also allows for a shorter transfer part, which has been reported to be the most time-consuming stage [17].

To achieve our goals, we apply optimal quantum control techniques to drive the system toward the desired state by minimizing the infidelity [18,21–25], a measure of the deviation between the target state and the state after the evolution of a particle moving from one optical trap to the next. Even though the engineered evolution path should by construction lead to a final state close to the desired one, there is no guarantee regarding the no-heating or no-loss condition, meaning that the system might be excited into the upper levels of the trap during the protocol and atoms may potentially be lost [26]. To solve this, we first analyze and characterize the performance of several tweezer trajectories used in state-of-the-art experiments (we consider four families: piecewise linear, minimum jerk, piecewise quadratic, and a hybrid between the linear and minimum-jerk ones [1,7,8,10–12,17]), with a particular focus on a measure of the error after transport and two measures of the vibrational excitations during transport as a function of the total time of the protocol.

In addition to considering experimentally motivated tweezer trajectories, we further develop a shortcuts-to-adiabaticity (STA) approach [15,27–31] to generate analytical pulses, which can also serve as a seed for subsequent optimization. More specifically, the STA method leverages a Hamiltonian invariant to derive pulses that drive the system in a nonadiabatic (or fast) way to the same final state as their adiabatic (or slow) counterparts [15,30]. The STA method provides great flexibility for computing the tweezer trajectory because it depends on ansatz functions that can be chosen freely, provided that they satisfy the necessary boundary conditions. When addressing the atom-transport problem, a wide variety of STA solutions have been derived for a harmonic trap or a power-law potential with time-independent frequency [15,25,31]. In our approach, we include the static-tweezer potential in the harmonic approximation to obtain solutions tailored to our specific setting. We show that our STA protocol outperforms the best experimentally inspired transport pulses, and our analytical approximation formulas can be straightforwardly implemented in experiments.

Following the characterization of the initial pulses, we carry out optimal pulse shaping using the user-friendly QuOCS toolkit [32]. Taking advantage of an expansion of the pulse over a randomized function basis, the included d-CRAB algorithm [33–36] allows for a drastic reduction of the number of free parameters to be optimized, so that a direct search method (such as Nelder-Mead) can be employed. At the same time, the need for computing the gradient of the control objective (or figure of merit) is alleviated. With this approach, low infidelities with respect to the target state were achieved, improving by more than one order of magnitude compared to the analytical pulse shapes. All the optimized pulses present a more stable behavior of the fidelity with respect to the target state after transport. Notably, while the optimized pulses reach an error threshold of 10^{-4} in a shorter total time compared to the nonoptimized experimentally motivated pulses (with reductions in time of 10%–30%), our proposed STA pulse requires the shortest time to obtain an error below 10^{-4}, and that time does not change after optimization. We interpret this as a signature of the high quality and suitability of our STA solution, as it approaches the numerically observed quantum speed limit (QSL) [18,37].

We aim to identify parameter regions of suitable pulses that can be used in the design of realistic experimental protocols. Thus, we choose the two pulses with the best performance and provide a heat map of the error after transport as a function of the total time and the depth of the moving tweezer. We determine a region in the parameter space for the minimum-jerk pulse leading to errors below 10^{-4} and certain *magical time windows* for the STA pulse where the error is suppressed by at least one order of magnitude [25]. In the investigated parameter interval, we observe that the performance of our STA pulse is almost independent of the moving-tweezer depth.

Finally, we identify a constraint on the choice of the total transport duration linked to the fundamental QSL of the system [18,37]. For an experimentally achievable moving-trap depth of about $3.57 \times 2\pi$ MHz and a transport distance of 7 μm, our results point toward a QSL of about 8 τ_{st} (here, for ^{39}K atoms, $\tau_{st} \approx 0.03$ ms is the characteristic time of the static tweezers, and this is related to that of the moving trap τ_{mt} via $\tau_{st} \approx 2\,\tau_{mt}$ for the considered maximum tweezer depth), a value that coincides with the time at which the population of vibrational states is equal to half of the states hosted by the trap. Although our obtained time threshold for the transport process is roughly five times larger than the one reported in Ref. [20], our results show a lower time threshold for the atom-transfer stage; in our case the time invested in the transfer stage is nine times smaller than the experimental time reported in Ref. [19]. Since the time required for capturing or releasing the atom was estimated to be 12 times larger than the time needed for the pure transport process [17], and the protocol of Ref. [20] does not include this time cost, our results highlight the importance of including the transfer between tweezers in the model.

The remainder of this paper is structured as follows. In Sec. II, we present our model for the atom-transport problem. In Sec. III, we describe the considered experimental pulses together with the method to generate analytical pulses by means of an STA procedure. In Sec. IV, we characterize the transport process for all the considered pulses and report the optimization results obtained using realistic experimental parameters. A summary and conclusions are given in Sec. V. Appendixes A–D provide details about the STA calculations, the numerical time evolution method, and the transport dynamics.

II. ATOM TRANSPORT IN AN EXTERNAL POTENTIAL

The transport of an atom in the presence of a static external potential $V_{\rm st}(x)$, from the initial position $x_{\rm i} = 0$ at time $t_{\rm i} = 0$ to the final position $x_{\rm f} = d$ at time $t_{\rm f} = T$ can be generically described by the Hamiltonian

$$H(x,t) = -\frac{\hbar^2}{2m}\frac{\partial^2}{\partial x^2} + V_{\rm mt}(x,t) + V_{\rm st}(x), \qquad (1)$$

where m is the mass of the atom. In current experiments, the external potential $V_{\rm st}(x)$ is typically generated either by a series of stationary optical tweezers, leading to a sum of Gaussian traps, or by counterpropagating laser beams, resulting in a sinusoidal pattern [1,8,9,14,38–43]. Here, we consider ^{39}K atoms with $m = 6.47 \times 10^{-26}$ kg, and we focus on static Gaussian traps, meaning that the external potential $V_{\rm st}(x)$ consists of a set of $n_{\rm st}$ time-independent Gaussian wells defined by the depth amplitude $A_{\rm st}/\hbar = 0.53 \times 2\pi$ MHz, width $\sigma_{\rm st} = 0.35$ µm, and minima positions $x^n_{\rm st} = (n-1)d$, with $d = 7$ µm being the distance between two adjacent minima of the periodic potential and $n = 1, 2, \ldots, n_{\rm st}$ [44]. To model the moving tweezer, we use a time-dependent Gaussian potential $V_{\rm mt}(x,t)$ and assume that the width of the tweezer is fixed to $\sigma_{\rm mt} = 0.47$ µm during the evolution [17,19,44,45]. Then, the control parameters for our problem are the amplitude of the moving tweezer $A_{\rm mt}(t)$ (trap depth) and the position of the center of the Gaussian well $x_{\rm mt}(t)$. The static and moving potentials are respectively

$$V_{\rm st}(x) = -A_{\rm st}\sum_{n=1}^{n_{\rm st}} \exp\left(-\frac{(x - x^n_{\rm st})^2}{2\sigma^2_{\rm st}}\right) \quad \text{and} \qquad (2a)$$

$$V_{\rm mt}(x,t) = -A_{\rm mt}(t)\exp\left(-\frac{(x - x_{\rm mt}(t))^2}{2\sigma^2_{\rm mt}}\right). \qquad (2b)$$

For the particle to be correctly transferred from the initial static tweezer to the moving one, transported through the total distance d, and then transferred to the final static tweezer, the following boundary conditions need to be satisfied:

$$\begin{aligned} &A_{\rm mt}(t_{\rm i}) = 0 \quad \text{and} \quad A_{\rm mt}(t_{\rm f}) = 0, \\ &x_{\rm mt}(t_{\rm i}) = x_{\rm i} = 0 \quad \text{and} \quad x_{\rm mt}(t_{\rm f}) = x_{\rm f} = d. \end{aligned} \qquad (3)$$

While the maximum amplitude for both the moving tweezer and the static traps are given by the power of the laser beams, the dynamics of the transport protocol depend on the trade-off between the static and moving amplitudes. Comparable amplitudes translate into a strong interaction between the moving and static tweezers, with the consequent oscillations of the atom in the traps that, in turn, lead to losses during transport. To prevent this from happening, we impose an extra condition on the amplitude during transport: $A_{\rm mt} > A_{\rm st}$, usually chosen as $A_{\rm mt} \approx 10A_{\rm st}$ [6,17,19].

Figure 1 presents a scheme of the atomic-transport protocol. The initial state $|\psi_{\rm i}\rangle$ and final target state $|\psi_{\rm tg}\rangle$ are the ground states, computed via exact diagonalization, of the static Hamiltonian with a single Gaussian potential centered at $x_{\rm i} = 0$ and $x_{\rm f} = d$, respectively. The goal is to determine the controls $x_{\rm mt}(t)$ and $A_{\rm mt}(t)$ such that the state after the complete time evolution, denoted by $|\psi(t_{\rm f})\rangle$, closely approximates the localized ground state of the final targeted trap $|\psi_{\rm tg}\rangle$. To quantify the error after the transport protocol, we compute the infidelity $\mathcal{I}(t_{\rm f}) = 1 - \mathcal{F}(t_{\rm f})$, where $\mathcal{F}(t)$ is the fidelity, which is defined as the overlap $\mathcal{F}(t) = |\langle\psi(t)|\psi_{\rm tg}\rangle|^2$. To shape the control pulses that execute the transport task with low infidelity, we first characterize the performance of several different pulse shapes based on current experimental realizations together with pulses that we derive within the STA formalism. In a second stage, we use these pulse profiles as initial guesses for optimal pulse shaping using the QuOCS toolkit, which allows us to reach even higher and more stable fidelities.

III. TRANSPORT PULSES

This section presents a theoretical description of the considered pulses. In Sec. III A, we describe the initial guesses motivated by experimental considerations. Section III B contains the analytical derivation of the STA solution.

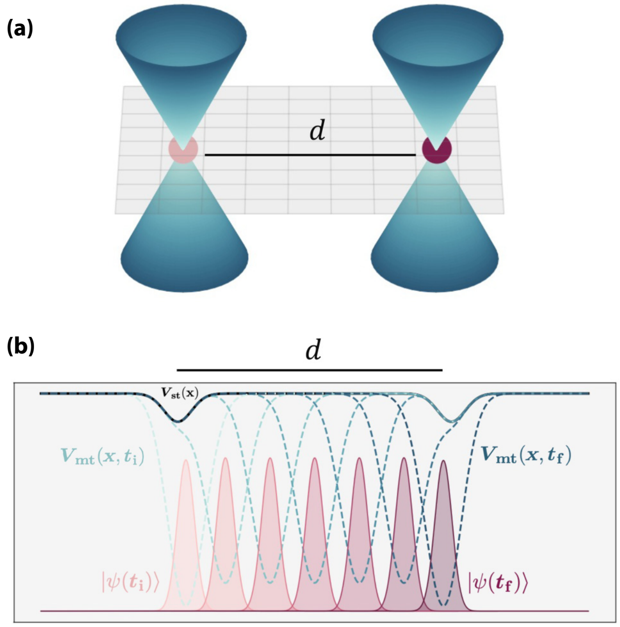

FIG. 1. Illustration of the transport protocol. (a) Two adjacent static tweezers (blue) separated by a distance d. (b) The atom initially trapped at $x_i = 0$ is transported to the position $x_f = d$ in a total time $T = t_f - t_i$. The amplitude of the external potential (static tweezers) denoted by $V_{st}(x)$ is shown as a solid black line, while that of the moving tweezer $V_{mt}(x, t)$ is depicted by dashed blue lines with a color gradient indicating the time evolution (from t_i to t_f lighter to darker—left to right). The probability of finding the particle in the position x is given by $|\psi(t)|^2$ and it is represented by the filled curves with a purple color gradient associated with the time arrow.

A. Pulses based on experiments

In current experiments, the choice of the ramps that control the position of the moving tweezer aims to suppress heating and losses, or equivalently, to minimize excitations during and after transport [1,7,8,10–12,17]. In our model, the control pulses time-dependently define the spatial trajectory followed by the bottom of the Gaussian trap $x_{mt}(t)$ and its depth, determined by the amplitude $A_{mt}(t)$. In practice, the minimum of the tweezer potential coincides with the focal spot [46], while the amplitude is proportional to the power of the beam [47]. The four transport trajectories based on current experiments that we consider are piecewise linear, piecewise quadratic, minimum jerk (derivative of the acceleration), and a hybrid trajectory that combines the linear and minimum-jerk ones. These are defined below.

The linear pulse, used for instance in Ref. [17], has the advantage of simplicity and the fact that the constant velocity can be implemented straightforwardly in experiments (using a constant sweep rate for the AOD frequency), but it is known to cause excitation due to the abrupt changes in the transport velocity at the discontinuity points. In the case of the piecewise-quadratic trajectory used in the experiments of Ref. [7], the atoms experience alternating accelerations of the same magnitude in the first and second half of the trajectory. This kind of quadratic pulse can be readily implemented with frequency-control systems [48]; however, the discontinuity in the acceleration might induce heating. The need for smooth position functions then arises to avoid unwanted excitations or energy excess. Although it was introduced in a completely different context (voluntary movements in primates [49]) 40 years ago, the minimum-jerk trajectory satisfies the latter requirement and was recently used to study diatomic molecule formation with the associated requirement of having not only the two atoms close enough but also in their relative motional ground state [10,11,19]. This trajectory minimizes the square of the jerk (derivative of the acceleration) over the full path, and it is also obtained when a polynomial ansatz is used to solve the position as a function of time for a translation with zero initial and final velocity and acceleration. In Ref. [10] the authors argue that the selection of the trajectory should aim to minimize heating due to jerk at the end points, and to avoid parametric heating due to trap depth oscillations [50]. The latter condition is further explained in Ref. [19]; when the frequency of the AOD is driven with a constant sweep rate (associated with a linear translation) resonant intensity modulations arising from imperfections in the AOD are avoided (see also Ref. [12]). A good compromise between preventing heating from changes in the acceleration at the beginning and end of the movement and at the same time avoiding resonant intensity modulations is found by using a hybrid pulse that implements a minimum-jerk trajectory for the start and end of the ramp and a constant-velocity (linear) translation for intermediate times.

As polynomial or piecewise-polynomial functions of time, the linear, quadratic, minimum-jerk, and hybrid trajectories have a simple analytical form. Since the target state in the final tweezer should closely match the initial state in the initial tweezer, and the considered static tweezers only differ in their position, one can chose symmetric "palindromic" pulses to reduce the degrees of freedom. In particular, the four families of experimentally motivated pulses that we consider are time-reversal symmetric. The linear trajectory x^l is given by

$$x^{l}(d,\tau,t) = d\frac{t}{\tau}, \tag{4}$$

where d is the distance covered and τ is the total time required for transport.

The piecewise-quadratic trajectory x^q, with a position described by two parabolas that intersect in the midpoint and have piecewise-constant acceleration, can be written as

$$x^{\mathrm{q}}(d,\tau,t) = d\begin{cases} 2\left(\frac{t}{\tau}\right)^2 & \text{for } 0 \le t \le \frac{\tau}{2}, \\ -2\left(\frac{t}{\tau}\right)^2 + 4\frac{t}{\tau} - 1 & \text{for } \frac{\tau}{2} \le t \le \tau. \end{cases} \tag{5}$$

In turn, the minimum-jerk trajectory x^{mj} reads

$$x^{\mathrm{mj}}(d,\tau,t) = d\left(10\left(\frac{t}{\tau}\right)^3 - 15\left(\frac{t}{\tau}\right)^4 + 6\left(\frac{t}{\tau}\right)^5\right), \tag{6}$$

where it is straightforward to check that the initial ($t = 0$) and final ($t = \tau$) velocity and acceleration are equal to zero.

Finally, the hybrid trajectory x^{hyb} is defined upon the fraction ξ of the total transport time that follows a linear motion. This fraction parameter is also called hybridicity [19]. Since the total time under linear motion $\xi\tau$ ranges between 0 and τ, we have $0 \le \xi \le 1$. Moreover, for $\xi = 0$, the trajectory reduces to the minimum-jerk trajectory, while for $\xi = 1$, the trajectory coincides with the piecewise-linear one, so it is reasonable to expect that when changing the parameter ξ, the dynamics of the system should interpolate between the dynamics under the linear and minimum-jerk pulses. The hybrid trajectory can be written as

$$x^{\mathrm{hyb}}(d,\tau,t) = \begin{cases} x^{\mathrm{mj}}\left(d\frac{8(1-\xi)}{8+7\xi}, \tau(1-\xi), t\right) & \text{for } 0 \le t \le \frac{1-\xi}{2}\tau, \\ d\left(\frac{15}{8+7\xi}\frac{t}{\tau} - \frac{7(1-\xi)}{2(8+7\xi)}\right) & \text{for } \frac{1-\xi}{2}\tau \le t \le \frac{1+\xi}{2}\tau, \\ x^{\mathrm{mj}}\left(d\frac{8(1-\xi)}{8+7\xi}, \tau(1-\xi), t-\tau\xi\right) + d\frac{15\xi}{8+7\xi} & \text{for } \frac{1+\xi}{2}\tau \le t \le \tau. \end{cases} \tag{7}$$

In Ref. [10], the experimental values of ξ are 0 and 0.95, i.e., a full minimum-jerk trajectory and a 95% linear one. The authors of Ref. [19] use $\xi = 0.1$ [see their Fig. 3(b)], value with which they report being able to avoid resonant intensity modulations for a translation of 4.5 μm and $\tau \approx$ 1.3 ms.

As mentioned before, we account not only for the transport process but also the transfer from the initial static trap to the moving tweezer and from the moving tweezer toward the target static one. Therefore, the protocol consists of three main stages: capturing the particle initially in the first static trap, the transport, and the final release of the particle in the target static tweezer. In the capturing stage, the depth of the moving tweezer is monotonically raised from zero to its maximum amplitude $A_{\mathrm{mt}}^{\max}$ while the position is kept constant. In the second transport stage, the position of the focal point follows one of the trajectories of Eqs. (4)–(7), while the power of the laser is kept constant, consistent with the experiments described in Ref. [11]. The third releasing stage is the inverse process of capturing: while maintaining the target position, the depth of the moving tweezer is decreased to zero. To assess the dynamics and quality of the final state, we add a fourth stage, which we call waiting time. During this time, the moving tweezer is off, and we evaluate several statistical measurements over the final state, mainly to examine its time stability and the possible presence of oscillations after transport (see for example Ref. [20]). Moreover, this waiting time can be used in the experiments to re-cool the atom before, for instance, the next concatenated transport step. The amplitude that we consider is then given by

$$A_{\mathrm{mt}}(t) = A_{\mathrm{mt}}^{\max}\begin{cases} \frac{3}{1-\eta}\frac{t}{T} & \text{for } 0 \le t \le \frac{1-\eta}{3}T, \\ 1 & \text{for } \frac{1-\eta}{3}T \le t \le \frac{1+2\eta}{3}T, \\ \frac{2+\eta}{1-\eta} - \frac{3}{1-\eta}\frac{t}{T} & \text{for } \frac{1+2\eta}{3}T \le t \le \frac{2+\eta}{3}T, \\ 0 & \text{for } \frac{2+\eta}{3}T \le t \le T, \end{cases} \tag{8}$$

where $t_{\mathrm{i}} = 0$ and $t_{\mathrm{f}} = T$. The total time T is divided into fractions defined by the parameter η, the transport time is assigned to be ηT, and the remaining time is divided into three intervals of equal length $(1-\eta)T/3$ for the capturing, releasing, and waiting stages. By doing so, we invest equal times for the capturing, releasing, and waiting stage. The obtained total position pulse is

$$x_{\mathrm{mt}}(t) = x_{\mathrm{i}} + \begin{cases} 0 & \text{for } 0 \leq t \leq \frac{1-\eta}{3}T, \\ x(d, \eta T, t - \frac{1-\eta}{3}T) & \text{for } \frac{1-\eta}{3}T \leq t \leq \frac{1+2\eta}{3}T, \\ d & \text{for } \frac{1+2\eta}{3}T \leq t \leq \frac{2+\eta}{3}T, \\ d & \text{for } \frac{2+\eta}{3}T \leq t \leq T, \end{cases} \tag{9}$$

where $x(d, \tau, t)$ denotes any of the trajectories defined in Eqs. (4)–(7).

The respective pulses are shown in Figs. 2(a) and 2(b). Figure 2(a) shows the amplitude obtained via Eq. (8) for a maximum amplitude $A_{\mathrm{mt}}^{\max}/\hbar = A_{\exp}/\hbar = 3.57 \times 2\pi$ MHz, $d = 7$ µm, $\eta = 2/5$, and $T = 2.5$ ms [45]. The start and end times of the transport stage are indicated as gray dashed vertical lines. Both controls $A_{\mathrm{mt}}(t)$ and $x_{\mathrm{mt}}(t)$ satisfy the boundary conditions specified by Eq. (3). While the amplitude for the experimentally motivated pulses is always a piecewise-linear function, all the trajectories have an s-shape position dependence. In Fig. 2(b), the piecewise-linear trajectory (solid magenta) and minimum-jerk trajectory (solid blue) are presented as the limiting cases of the hybrid trajectory, which is depicted for several ξ values (gradient from magenta to purple). The minimum-jerk trajectory has the smallest velocity at the beginning (for details about the differences between the pulses at the beginning of the transport interval, see the insets of Fig. 2 depicting enlarged views of the pulses for times between 0.5 and 1 ms and positions between 0 and 1 µm) and at the end of the transport and reaches the highest one at the middle time point. For the hybrid pulse, the change ratio at the beginning and at the end of the transport decreases for decreasing hybridicity ξ. The quadratic pulse (dashed yellow line) has a higher velocity in the first and final part of the transport when compared to the minimum-jerk one, and it also has a slightly higher velocity in the middle time or inflection point.

B. Shortcut-to-adiabaticity solution

Since the piecewise-linear, hybrid, minimum-jerk, and quadratic control pulses are experimentally inspired ansätze for transport, they do not include the specifics of the system, which are encoded in the Hamiltonian of Eq. (1). In particular, there is no consideration of the shape of the moving tweezers $V_{\mathrm{mt}}(x, t)$, let alone the presence of the static tweezers $V_{\mathrm{st}}(x)$ in the background [see Eq. (2)]. To derive pulses that solve the fast-transport problem taking into account these effects while offering flexibility for satisfying desirable and realistic boundary conditions, we draw upon the STA framework. The main idea of STA methods is to develop protocols that lead to the same final state as their adiabatic (slow) counterpart in considerably shorter times [51], enabling us to avoid noise and decoherence effects.

The minimum-jerk trajectory was proposed to perform a translation of the minimum point of a perfect harmonic oscillator with minimal motional excitation at the beginning and end of the transport by constraining the velocity and acceleration to be zero at the initial and final times (see for instance Refs. [15,25,52]). Here, we use the minimum-jerk functional form in intermediate steps of the derivation of a new set of controls $A_{\mathrm{mt}}(t)$ and $x_{\mathrm{mt}}(t)$, which take into account the specific form of the moving and static tweezers. While several STA-based approaches for atom transport have been proposed [15,25,31,53–57], to the best of our knowledge, the background of static tweezers has not previously been incorporated into an STA solution. To address a more realistic scenario, we derive an STA control pulse that includes the transfer between optical tweezers in the transport, therefore avoiding errors during this critical stage.

The first step in our approach is to approximate the Hamiltonian of Eq. (1) with a time-dependent harmonic oscillator and then use known results on fast eigenstate transfer for the harmonic case [15,58]. In this way, the time-dependent oscillator accounts for both the static and moving tweezers. We start by expanding the complete potential in a Taylor series up to the second order around the center of the moving tweezer $x_{\mathrm{mt}}(t)$. By completing the resulting polynomial in x to a square form and ignoring a time-dependent energy offset, we obtain a

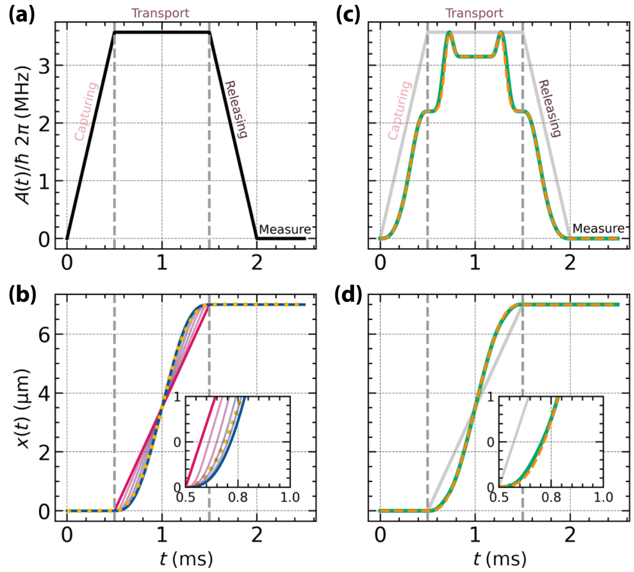

FIG. 2. Control pulses: position $x_{\mathrm{mt}}(t)$ and amplitude $A_{\mathrm{mt}}(t)$. The depth of the moving tweezer or amplitude control is shown in panels (a) and (c), while the position of the minimum of the moving trap is shown in panels (b) and (d) for a total time of a total time of $T = 2.5$ ms, a maximum amplitude $A_{\mathrm{mt}}^{\mathrm{max}}/\hbar = 3.57 \times 2\pi$ MHz, a transport time ηT with $\eta = 2/5$, and a total distance between static tweezers $d = 7$ μm. The start and end of the transport stage are indicated by gray dashed vertical lines. (a) Piecewise amplitude ramp consisting of four stages: transferring the atom from the initial static tweezer to the moving one, transport, transferring the atom from the moving tweezer to the target static one, and a final waiting or measuring time, see Eq. (8); (b) Position of the moving tweezer as a function of time for a piecewise-linear (magenta), minimum-jerk (blue), and quadratic (yellow dashed line) pulses [see Eqs. (4)–(6)]. The linear and minimum-jerk trajectories are particular cases of the more general hybrid pulse given in Eq. (7), which is also depicted for hybridizations $\xi = 0.2$, 0.4, 0.6, and 0.8 (curves with color gradients from blue to magenta; see insets for details of the position control at the beginning of the transport stage). The velocity of the moving tweezer at the beginning and end of the transport interval decreases with ξ and is minimum for the minimum-jerk pulse. (c) Amplitude shape calculated within the STA approach, showing the full numerical solution (solid turquoise curve) and the approximation obtained using Eq. (21) (dashed orange line). The piecewise-linear amplitude associated with the piecewise-linear, hybrid, minimum-jerk, and quadratic ramps is shown as a light gray curve to highlight that the maximum amplitude is the same for all pulses. The two peaks at maximum amplitude depicted by the STA pulse are developed to counteract the restoring force of the static tweezers. (d) Full numerical and approximated position of the moving tweezer obtained with the STA formalism, same color code as in panel (c).

moving harmonic oscillator with a time-dependent effective frequency

$$H_0(x,t) = -\frac{\hbar}{2m}\frac{\partial^2}{\partial x^2} + \frac{m\omega(t)^2}{2}[x - x_0(t)]^2, \tag{10}$$

where $\omega(t)$ and $x_0(t)$ are related to the controls and the derivatives of the static potential through

$$m\omega^2(t) = \left.\frac{d^2 V_{\mathrm{st}}}{dx^2}\right|_{x_{\mathrm{mt}}(t)} + \frac{A_{\mathrm{mt}}(t)}{\sigma_{\mathrm{mt}}^2}, \tag{11}$$

and

$$x_0(t) = x_{\mathrm{mt}}(t) - \frac{\left.\frac{dV_{\mathrm{st}}}{dx}\right|_{x_{\mathrm{mt}}(t)}}{m\omega^2(t)}. \tag{12}$$

For the time-dependent Hamiltonian of Eq. (10), it is possible to construct a dynamical invariant $I(x,t)$ such that for any wave function $\psi(t)$ evolving with $H_0(x,t)$, we have $(\mathrm{d}/\mathrm{d}t)\langle\psi(t)|I(t)|\psi(t)\rangle = 0$. This means that with the appropriate time dependence of $\omega(t)$ and $x_0(t)$, if the system is initially in an eigenstate of $H_0(t_{\mathrm{i}})$, the time evolution will map it onto the corresponding eigenstate of $H_0(t_{\mathrm{f}})$ (see Appendix A for details). For our particular form of $H_0(x,t)$, the dynamical invariant involves two auxiliary functions $\alpha(t)$ and $\rho(t)$ that satisfy

$$x_0(t) = \frac{\ddot{\alpha}(t)}{\omega^2(t)} + \alpha(t) \quad \text{and} \tag{13}$$

$$\omega^2(t) = \frac{\omega_0^2}{\rho^4(t)} - \frac{\ddot{\rho}(t)}{\rho(t)}, \tag{14}$$

where ω_0 is a free constant. From the first of these equations, we see that $\alpha(t)$ can be identified with a classical trajectory of a driven generalized classical harmonic oscillator [59], and $\rho(t)$ can be seen as a spatial rescaling factor. While Eqs. (13) and (14) ensure that $H_0(x,t)$ has fast transport modes given by the eigenstates of $I(t)$ up to a phase, we also need them to coincide with the eigenstates of $H_0(x,t)$ at the initial and final times. To fulfill the latter requirement, the two auxiliary functions must also satisfy the following boundary conditions:

$$\dot{\alpha}(t_{\mathrm{i}}) = \ddot{\alpha}(t_{\mathrm{i}}) = \dot{\alpha}(t_{\mathrm{f}}) = \ddot{\alpha}(t_{\mathrm{f}}) = 0 \quad \text{and} \tag{15}$$

$$\dot{\rho}(t_{\mathrm{i}}) = \ddot{\rho}(t_{\mathrm{i}}) = \dot{\rho}(t_{\mathrm{f}}) = \ddot{\rho}(t_{\mathrm{f}}) = 0. \tag{16}$$

The strategy to obtain the desired pulse is essentially reverse engineering. First, we choose $\alpha(t)$ and $\rho(t)$ satisfying the boundary conditions, which we then use to compute $x_0(t)$ and $\omega(t)$ using Eqs. (13) and (14). After that, we numerically solve Eq. (12) to find the position of the moving tweezer $x_{\mathrm{mt}}(t)$, which is finally plugged into Eq. (11) to obtain the tweezer amplitude $A_{\mathrm{mt}}(t)$.

A simple way to design functions satisfying boundary conditions on the derivatives such as those of Eqs. (15) and (16) is to look for an appropriate polynomial function [15,52,53,60]. This polynomial interpolation has the advantage that most of the calculations can be carried out analytically. As already mentioned, the lowest-order polynomial in a variable s having vanishing first and second derivative at the initial and final points ($s = 0, 1$) is given by the minimum-jerk polynomial $p_{\rm mj}(s) = 10s^3 - 15s^4 + 6s^5$ (notice that $p_{\rm mj}(0) = 0$ and $p_{\rm mj}(1) = 1$); therefore, we choose both $\alpha(t)$ and $\rho(t)$ to have the functional form of $p_{\rm mj}$ with suitable multiplicative and additive constants. Because our transport protocol is divided into stages, we apply the reverse-engineering process to each time interval and require continuous outputs. In other words, for each stage, we propose $\alpha(s) = \alpha_{\rm i} + p_{\rm mj}(s)(\alpha_{\rm f} - \alpha_{\rm i})$ and $\rho(s) = \rho_{\rm i} + p_{\rm mj}(s)(\rho_{\rm f} - \rho_{\rm i})$, where $s = t/(t_{\rm f} - t_{\rm i})$ is the dimensionless time and the i and f subscripts denote initial and final values over the considered interval. Using this form for the auxiliary functions, Eqs. (15) and (16) are satisfied for any $\alpha_{\rm i,f}$ and $\rho_{\rm i,f}$, which are to be fixed by the initial and the target position and by requiring the physical controls to be continuous functions of time.

We now turn to the calculation of the auxiliary functions. As mentioned before, for the proposed form for $\alpha(t)$, it is easy to see that $\ddot{\alpha}(t)$ vanishes at the initial and the final time of each stage, i.e., for $t = 0$, $(1 - \eta)T/3$, $(1 + 2\eta)T/3$, $(2 + \eta)T/3$, and T; therefore, for those values of time, we have $\alpha(t) = x_0(t)$. Since the position of the moving optical tweezer $x_0(t)$ only changes during the transport interval, the calculation of $\alpha(t)$ is straightforward and leads to

$$\alpha(t) = d \begin{cases} 0 & \text{for } 0 \le t \le \frac{1-\eta}{3}T, \\ 10\left(\frac{t - \frac{(1-\eta)}{3}T}{\eta T}\right)^3 - 15\left(\frac{t - \frac{(1-\eta)}{3}T}{\eta T}\right)^4 + 6\left(\frac{t - \frac{(1-\eta)}{3}T}{\eta T}\right)^5 & \text{for } \frac{1-\eta}{3}T \le t \le \frac{1+2\eta}{3}T, \\ 1 & \text{for } \frac{1+2\eta}{3}T \le t \le \frac{2+\eta}{3}T, \\ 1 & \text{for } \frac{2+\eta}{3}T \le t \le T. \end{cases} \tag{17}$$

To compute the auxiliary function $\rho(t)$, it is useful to define the frequency associated with the static traps

$$\omega_{\rm st} = \sqrt{\frac{1}{m}\left.\frac{d^2V_{\rm st}}{dx^2}\right|_{x=0,d}} = \sqrt{\frac{A_{\rm st}}{m\sigma_{\rm st}^2}}, \tag{18}$$

and the maximum frequency for the moving tweezer over the capturing and releasing intervals, which is the same as the initial frequency in the transport interval and is given in terms of the maximum depth of the moving tweezer over the capturing (c) or releasing (r) stages $A_{\rm mt}^{\rm max,cr}$:

$$\omega_{\rm mt}^{\rm max,cr} = \sqrt{\frac{A_{\rm mt}^{\rm max,cr}}{m\sigma_{\rm mt}^2}}. \tag{19}$$

Notice that in the case of the experimentally inspired pulses described in the previous section, $A_{\rm mt}^{\rm max,cr}$ matches the global maximum amplitude of the pulse $A_{\rm mt}^{\rm max}$. At the beginning of the capturing stage, at the end of the releasing interval, and at the end of the protocol (i.e., for $t = 0$, $(2 + \eta)T/3$, and T), the moving tweezer is completely off, and we therefore have $\omega(t) = \omega_{\rm st}$ [see Eq. (11)].

In contrast, at the end of the capturing interval and at the beginning of the releasing interval, i.e., for $t = (1 - \eta)T/3$ and $(1 + 2\eta)T/3$, the amplitude of the moving tweezer is at its maximum value over the capturing or releasing stage, meaning that $\omega(t) = \sqrt{\omega_{\rm st}^2 + (\omega_{\rm mt}^{\rm max,cr})^2}$. Using this in Eq. (14), we get

$$\rho(t) = \frac{\sqrt{\omega_0}}{\sqrt{\omega_{\rm st}}} \begin{cases} 1 + \left(\frac{1}{\sqrt[4]{\tilde{\omega}^2+1}} - 1\right)\left\{10\left(\frac{t}{\frac{(1-\eta)}{3}T}\right)^3 - 15\left(\frac{t}{\frac{(1-\eta)}{3}T}\right)^4 + 6\left(\frac{t}{\frac{(1-\eta)}{3}T}\right)^5\right\} & \text{for } 0 \le t \le \frac{1-\eta}{3}T, \\ \frac{1}{\sqrt[4]{\tilde{\omega}^2+1}} & \text{for } \frac{1-\eta}{3}T \le t \le \frac{1+2\eta}{3}T, \\ \frac{1}{\sqrt[4]{\tilde{\omega}^2+1}} - \left(\frac{1}{\sqrt[4]{\tilde{\omega}^2+1}} - 1\right)\left\{10\left(\frac{t - \frac{(1+2\eta)}{3}T}{\frac{(1-\eta)}{3}T}\right)^3 - 15\left(\frac{t - \frac{(1+2\eta)}{3}T}{\frac{(1-\eta)}{3}T}\right)^4 + 6\left(\frac{t - \frac{(1+2\eta)}{3}T}{\frac{(1-\eta)}{3}T}\right)^5\right\} & \text{for } \frac{1+2\eta}{3}T \le t \le \frac{2+\eta}{3}T, \\ 1 & \text{for } \frac{2+\eta}{3}T \le t \le T, \end{cases} \tag{20}$$

with $\tilde{\omega}^2 = (\omega_{\rm mt}^{\rm max,cr}/\omega_{\rm st})^2 = A_{\rm mt}^{\rm max,cr}\sigma_{\rm st}^2/(A_{\rm st}\sigma_{\rm mt}^2)$. Now that we have the expression for $\rho(t)$, the calculation of $\omega(t)$ is straightforward via Eq. (14). The resulting $\omega(t)$ can be used together with $\alpha(t)$ in Eq. (13) to obtain $x_0(t)$. It is important to note that since $\rho(t) \propto \sqrt{\omega_0}$, and also because $\alpha(t)$ does not depend on this quantity, $\omega(t)$ (and as a consequence $x_0(t)$) are independent of ω_0. After that, the obtained $x_0(t)$ is plugged into Eq. (12), and the equation is numerically solved to get $x_{\rm mt}(t)$, which we then use in Eq. (11) to derive the amplitude control $A_{\rm mt}(t)$.

The numerical solutions for the amplitude and the position of the bottom of the moving trap are shown in Figs. 2(c) and 2(d) as solid turquoise curves. To compare these engineered solutions with the pulses described in the previous section, we superimpose the piecewise-linear pulse and the piecewise-linear amplitude as light-gray solid curves. Note that the inset of Fig. 2(d) provides an enlarged view of the pulses for times between 0.5 and 1 ms and positions between 0 and 1 μm. While $x_0(t)$ strongly resembles the minimum-jerk trajectory, the amplitude presents two peaks that counteract the effect of the static tweezers during the atom-transport task and are directly related to the second-derivative term in Eq. (11) (see also Appendix A). For a general problem, the quantity and spacing of these peaks will be given by both the number of static traps and the spatial separation between them. In most experimental implementations, the power of the laser that generates the moving tweezer is kept constant during the movement (see for instance Ref. [11] or Fig. 9 of Ref. [19]), as we already consider for the piecewise-linear, hybrid, minimum-jerk, and quadratic ramps; however, in the supplemental material of Ref. [8], the authors mention that when transferring from the static to the moving tweezers, they use a quadratic intensity profile, highlighting the possibility of implementing our STA amplitude pulse.

Before moving to the next section, we provide a quite simple and directly applicable analytical approximation for the STA controls. The approximated solutions can be obtained using a quadratic approximation for the external potential, $V_{\rm st}(x) \approx -A_{\rm st}(1-2x/d)^2$, which is only valid between the two minima, i.e., for $0 \le x \le d$. Within this approximation, we get

$$x_{\rm mt}(t) \approx \frac{x_0(t) + \frac{4A_{\rm st}}{dm\omega^2(t)}}{1 + \frac{8A_{\rm st}}{d^2 m\omega^2(t)}}, \tag{21}$$

an expression that when combined with Eq. (11) leads to an approximated solution for $A_{\rm mt}(t)$. It is important to note that, for this approximated $x_{\rm mt}(t)$, the boundary conditions are also approximately fulfilled. In the transport interval, the approximated solution can be written as

$$x_{\rm mt}(t) \approx d\frac{10\left(\frac{t-\frac{1-\eta}{3}T}{\eta T}\right)^3 - 15\left(\frac{t-\frac{1-\eta}{3}T}{\eta T}\right)^4 + 6\left(\frac{t-\frac{1-\eta}{3}T}{\eta T}\right)^5 + \frac{60\left(\left(\frac{t-\frac{1-\eta}{3}T}{\eta T}\right) - 3\left(\frac{t-\frac{1-\eta}{3}T}{\eta T}\right)^2 + 2\left(\frac{t-\frac{1-\eta}{3}T}{\eta T}\right)^3\right)}{(\eta T)^2\left(\frac{A_{\rm st}}{m\sigma_{\rm st}^2} + \frac{A_{\rm mt}^{\rm max,cr}}{m\sigma_{\rm mt}^2}\right)} + \frac{4A_{\rm st}}{d^2\left(\frac{A_{\rm st}}{\sigma_{\rm st}^2} + \frac{A_{\rm mt}^{\rm max,cr}}{\sigma_{\rm mt}^2}\right)}}{1 + \frac{8A_{\rm st}}{d^2\left(\frac{A_{\rm st}}{\sigma_{\rm st}^2} + \frac{A_{\rm mt}^{\rm max,cr}}{\sigma_{\rm mt}^2}\right)}}. \tag{22}$$

A direct evaluation of the coefficients of the second and third terms of the numerator, as well as the second term in the denominator, leads to values below 10^{-3}, meaning that the STA trajectory closely resembles the minimum-jerk one. Importantly, with the same Taylor expansion, we also derived an approximation for the maximum amplitude of the STA pulse in terms of the maximum amplitude over the capturing or releasing stage (or, equivalently, the initial amplitude in the transport interval), $A_{\rm mt,STA}^{\rm max} \approx A_{\rm mt}^{\rm max,cr} + A_{\rm st}(1+2/e^{3/2})\sigma_{\rm mt}^2/\sigma_{\rm st}^2 \ge A_{\rm mt}^{\rm max,cr}$. The latter expression allows us to compare pulses with the same global maximum amplitude, which is the relevant experimental parameter. The approximations obtained for the STA control pulses using the same experimentally realistic values for the parameters as in the previous sections are depicted in Figs. 2(c) and 2(d) as dashed orange lines. We checked that the approximation for the maximum amplitude of the STA ramp presents a very good agreement with the full numerical results, and also that the relative error between the full numerical solution and the approximation for the amplitude is less than 4% during the transport interval.

In a recent work, Hwang *et al.* experimentally demonstrated the advantage of an STA-based trajectory over the constant-velocity and constant-jerk trajectory [61]. Also using STA techniques and a harmonic truncation of the tweezer potential, Jaewook Ahn's team developed a trajectory very similar to that given in Eqs. (21) and (22), and they demonstrated that the STA survival probability of atoms after transportation outperforms the non-STA ones. We would like to highlight that even though our approaches are similar, there are two key differences: first, their calculations consider only the moving tweezer and not the static ones, and second, they do not develop the amplitude pulse to make use of the depth of the tweezer as a second control variable. To compare both STA approaches, we simulate the transport protocol using the trajectory described in Ref. [61] for a total distance of 7 μm and $A_{\text{mt}}^{\max}/\hbar = 3.57 \times 2\pi$ MHz. For a protocol time of 2.5 ms, we obtain an infidelity of 1.5×10^{-5}, to be compared with the minimum-jerk infidelity of 1.4×10^{-5} and the one for our full STA solution of 5.3×10^{-6}; moreover, the infidelity obtained with our STA approach is one order of magnitude below the infidelity reported in Ref. [61] for total pulse times in the range $[0.01, 3]$ ms. As we show in the next section, incorporating a modulation into the amplitude of the moving tweezer that counteracts the restoring force of the static traps allows the STA pulse to outperform the experimentally motivated ones, even without optimization. We trust that the simple approximations for our STA solutions provided in this section will motivate their experimental implementation in the near future [62].

IV. ATOM TRANSPORT CHARACTERIZATION AND OPTIMIZATION

In this section, we present a performance analysis of the considered pulses and their subsequent optimization.

A. Performance of the closed-form pulses

To evaluate the performance of the transport of a single atom under the piecewise-linear, hybrid, minimum-jerk, quadratic, and STA pulses, we are mainly concerned with two features: first, that the transport is faithful (high-fidelity condition), and second, that the vibrational excitations of higher states are reasonably bounded to prevent atom losses [63,64]. To check the first condition, we analyze the transport infidelity. As explained in Sec. II, the infidelity quantifies the error after the transport, and it is closer to zero when the state of the atom is closer to the target state. Since our target state is the ground state of the target tweezer, a lower infidelity at the end of the transport is equivalent to limited heating after the complete transport protocol.

Since the potential of an optical tweezer has finite depth, it is also necessary to assess whether the no-heating condition is satisfied during transport. As discussed in Ref. [64], the main effect of heating is to expel the atom from the trap not as a result of an increase in the mean energy but as a consequence of the spreading of the width of the distribution over the energy states (the physical picture is that when the upper tail of the distribution reaches untrapped levels, the atom is lost). Based on this argument, to quantify the increase in the vibrational quantum number, we calculate the mean value $\langle N \rangle$ and the width ΔN of the distribution of the atomic state over the instantaneous eigenstates of the moving tweezer. Following Ref. [65], we also calculate an effective temperature given by the expectation value of the kinetic operator $T_{\text{eff}} = 2\langle K \rangle / k_B$, with k_B denoting the Boltzmann constant and $K = p^2/(2m)$, where p is the momentum operator. By means of the virial theorem for a harmonic trap, we have $\langle H \rangle = 2\langle K \rangle$ [66]. Thus, T_{eff} is a measure of the mean energy of the system, which is usually reported to analyze the stability of the system during transport [25,56]. In our case, the maximum depth of the moving tweezer during transport hosts about 55 oscillator levels, and the deviation of the lower states with respect to the harmonic ones is small. In the following, we use Système International (SI) units and characteristic units for the time; from the frequency of the static potential [see Eq. (18)], we can define a characteristic time as $\tau_{\text{st}} = 2\pi/\omega_{\text{st}} \approx 0.03$ ms. We use this value, since it is fixed for any maximum amplitude of the moving tweezer; however, the relationship between this value and the characteristic time during transport is $\tau_{\text{mt}} = 2\pi/\omega_{\text{mt}}^{\max} \approx \tau_{\text{st}}/2$.

The infidelity as a function of the total time T is reported in Fig. 3 for the piecewise-linear, hybrid ($\xi = 0.8, 0.4$), minimum-jerk, quadratic, and STA (full numerical solution and approximation) pulses from left to right. We consider total times ranging between 0.01 and 3 ms, in agreement with the experimental values (see for instance Ref. [10] or Ref. [19]). We calculate the maximum (solid curve), average (dashed line), and last value (dotted line) of the infidelity over the final interval of the pulse. Since it constitutes an upper bound, we propose the maximum value as the quantity to be used when comparing with experimental results. The shaded area corresponds to one standard deviation as a measure of the error in the fidelity.

As expected, the piecewise-linear pulse produces the highest error after transport (with an infidelity higher than 10^{-2} for all T) and sustained oscillations (with a period of about $12\,\tau_{\text{st}}$). The hybrid-pulse behavior interpolates between the minimum-jerk and the linear behavior and presents more oscillations for higher ξ (i.e., going toward the linear ramp, as expected). The quadratic-pulse infidelity has a similar behavior to that of the hybrid pulse with $\xi \lesssim 0.5$ but with a slightly higher oscillatory behavior. Among all the pulses, the minimum-jerk and the STA ones present the smoothest and most stable behavior. Moreover, the STA pulse also enables reaching the lowest infidelity in the shortest time; the infidelity rapidly decreases for T between 10 and $20\,\tau_{\text{st}}$ and then reaches a stable value around 10^{-4}. In general, we observe that all the pulses fail in the transport task for $T \lesssim 10\,\tau_{\text{st}}$. For total times greater than $10\,\tau_{\text{st}}$, the infidelity decreases when the total time increases, and the hybrid, minimum-jerk, quadratic,

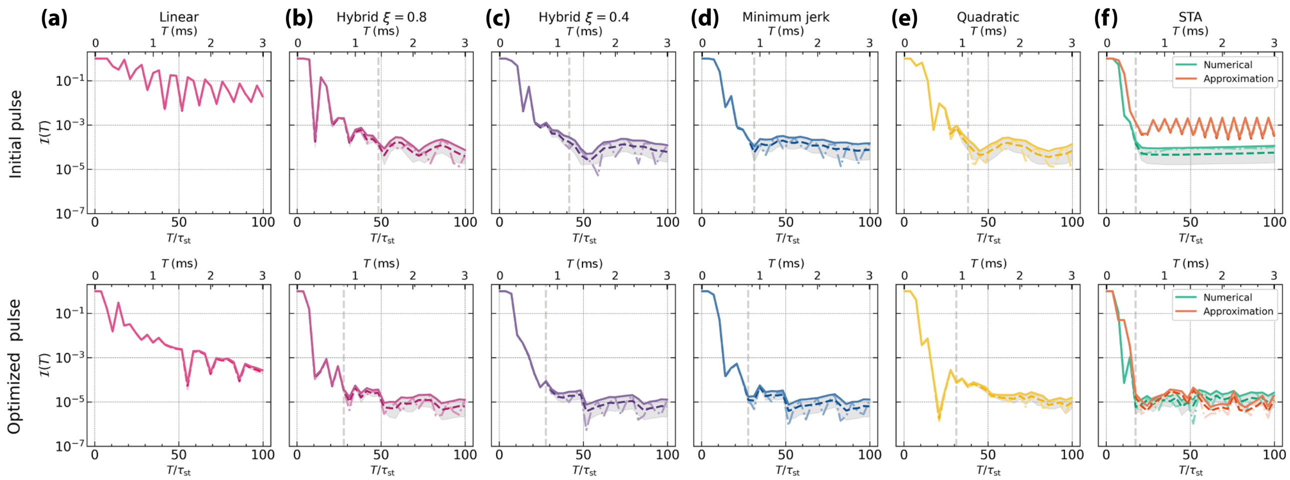

FIG. 3. Error after transport. Infidelity $\mathcal{I}$ versus total time T for the initial (top) and optimized (bottom) pulses with: (a) piecewise linear; hybrid with (b) $\xi = 0.8$ and (c) $\xi = 0.4$; (d) minimum jerk; (e) quadratic; and (f) STA. All the pulses have a maximum amplitude of $A_{\mathrm{mt}}^{\max}/\hbar = 3.57 \times 2\pi$ MHz, the transport time is given by $\eta\, T$ with $\eta = 2/5$, and the total distance between static tweezers is $d = 7\ \mu$m. The maximum, average, and last value of the infidelity over the last stage of the protocol [see Eqs. (8) and (9)] are shown as solid, dashed, and dotted lines, respectively. The shaded area indicates the standard deviation calculated over the same time interval and quantifies the error in the infidelity. The vertical gray dashed line highlights the value of the total time for which the infidelity reaches the threshold of 10^{-4}. For the hybrid pulse with $\xi = 0.8$ and 0.4, minimum-jerk, quadratic, and STA ramps, the corresponding times are approximately 48 τ_{st}, 41 τ_{st}, 31 τ_{st}, 38 τ_{st}, and 18 τ_{st}, with τ_{st} being the characteristic time of the static traps (the characteristic time during transport is $\tau_{\mathrm{mt}} \approx \tau_{\mathrm{st}}/2$). For the two hybrid and minimum-jerk optimized pulses, these times decrease to 28 τ_{st}, the time for the quadratic ramp decreases to 31 τ_{st}, the STA threshold time does not change, and the piecewise-linear optimized pulse reaches the infidelity threshold for a total time of approximately 55 τ_{st}. For the considered total pulse times and distance, the range for the mean velocity during transport goes from 1.75 m/s at a total protocol time of 0.01 ms to 5×10^{-3} m/s for a total time of 3 ms.

and STA pulses present two more regimes: a diabatic regime with some oscillations between $T \approx 10\,\tau_{\mathrm{st}}$ and a value in the range 20–50 τ_{st}, and the adiabatic regime for sufficiently large T. The total time at which the second regime ends depends on the pulse and corresponds in increasing order to the ramps for STA, minimum jerk, hybrid with $\xi = 0.4$, quadratic, and hybrid with $\xi = 0.8$. After that, the fidelity saturates with some smooth oscillations that improve when the upper time threshold of the diabatic regime decreases. Interestingly, the STA approximation captures the two first regimes well, including the value of the diabatic threshold, but it presents strong oscillations with a period of about 8 τ_{st} in the last adiabatic regime. For total times $T \gtrsim 50\,\tau_{\mathrm{st}}$, the hybrid, minimum-jerk, quadratic, and STA pulses reach the adiabatic regime, and therefore, any of those pulses can faithfully perform the transport task.

Since the STA ramp presents a clear advantage for short T, we conclude that our proposed STA protocol has the best performance, achieving the infidelity threshold of 10^{-4} (vertical dashed line) in nearly half of the time taken by the minimum-jerk trajectory (which is the second-best one). Moreover, using the fidelity as a measure of the probability of a faithful transport process between two tweezers and assuming independent transport processes (see Ref. [61]) between tweezers, we can estimate the fidelity after a transport protocol involving n_{st} traps. For instance, using the infidelity obtained for our STA solution for a typical experimental transport velocity of 10 nm/μs [17], we obtain an infidelity of 10^{-2} after 30 consecutive independent transport movements. In Appendix C, we present examples of the evolution of the infidelity for total pulse durations $T = 0.5$, 1.5, 2.5, and 3 ms, while in Appendix D, we report the infidelities for various total distances and total pulse times, as well as their dependence on the velocity.

To test the performance of the STA solutions in a different experimental setting, we compute the pulses and simulate the evolution using the parameter values described in Ref. [17]. Our proposed STA solutions (both fully numerical and approximate) allow us to complete the transport and transfer between two neighboring tweezers separated by a distance of 5 μm in 160 μs with an infidelity of about 10^{-4}. Comparing this time to a total time of 1.25 ms reported in Ref. [17], our pulse performs the task 7.8 times faster, even when the transport stage is carried out more slowly (for us, it takes 80 μs, while in the experiments of Ref. [17], it takes 50 μs). More strikingly, our STA protocols reduce the transfer time devoted to capturing or releasing from and to static traps by a factor of 15 (in our case 40 μs, versus 600 μs for the experiments reported in Ref. [17]). We would like to stress that these results could be further improved by adapting the ratio between the time devoted to the transport and transfer stage to parameters of the system at hand.

Figure 4 depicts the maximum expected value $\max(\langle N \rangle)$ and the associated uncertainty or width of the distribution $\max(\Delta N)$ for the occupied states of the moving tweezer, together with the maximum effective temperature $\max(T_{\rm eff})$ as a function of the total pulse time T [67]. As expected, both quantities increase for shorter T because diabatic processes induce a higher mixture of states. The increase in the vibrational modes shows a similar behavior for all the considered pulses; for total times above 0.5 ms, the wave function has a dominant weight over the ground state of the moving trap and smaller weights over the first and second excited states. For total pulse times shorter than 0.5 ms, the expectation value of the occupied moving tweezer states $\langle N \rangle$ and its uncertainty ΔN increase rapidly for decreasing total times. For $T \approx 0.22$ ms $\approx 8\,\tau_{\rm st}$, the mean occupied level plus the associated uncertainty reaches half of the trap states, i.e., 27 levels for our trap hosting a total of 55 states. An estimation of the vibrational number increase for a moving harmonic oscillator can be obtained by evaluating the Fourier transform of the acceleration at the frequency of the oscillator [1,56,68]. By computing the Fourier transform of the acceleration of our approximated STA trajectory [Eq. (22)], we find an agreement with less than 10% of relative difference between the time at which our protocol reaches an increase of 27 oscillator levels and the time that would be needed by the STA solution proposed by Jaewook Ahn's group; see Eq. (7) of Ref. [61].

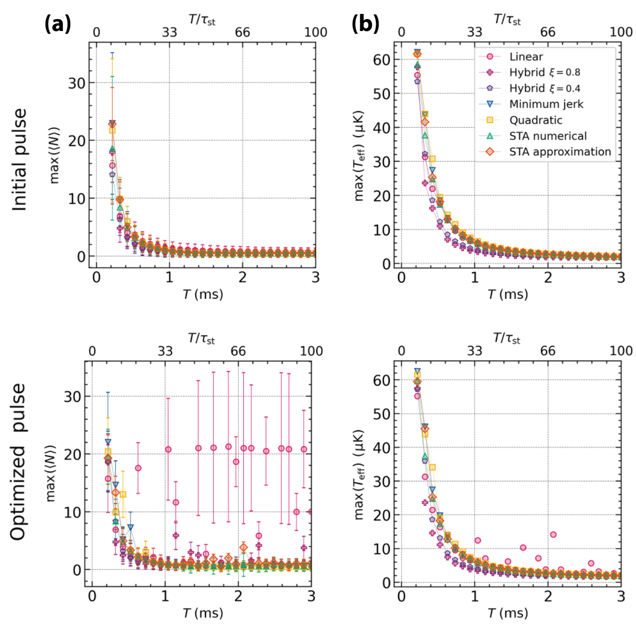

FIG. 4. Upper-bound measures of heating during transport. (a) Maximum of the mean occupied level (points) and width (error bars) of the distribution over the moving-tweezer states (denoted respectively by $\langle N \rangle$ and ΔN). (b) Maximum effective temperature $T_{\rm eff}$ over the complete duration of the pulse as a function of the total time T for the initial pulses (top row) and the optimized ones (bottom row). The measures obtained for the piecewise-linear, hybrid with $\xi = 0.8$ and $\xi = 0.4$, minimum-jerk, quadratic, and STA (fully numerical solution and approximation) ramps are depicted as magenta circles, burgundy crosses, purple pentagons, blue down-pointing triangles, yellow squares, turquoise up-pointing triangles, and orange diamonds, respectively, with a line of the same color as a guide for the eye. For a total pulse time of $T \approx 0.22$ ms $\approx 8\,\tau_{\rm st}$, the mean occupied level plus its uncertainty is equal to half of the states hosted by the moving tweezer. All the initial pulses have a maximum amplitude of $A_{\rm mt}^{\rm max}/\hbar = 3.57 \times 2\pi$ MHz, a transport time of ηT with $\eta = 2/5$, and a total distance $d = 7$ μm. As before, $\tau_{\rm st}$ denotes the characteristic time of the static traps, and this is related to the characteristic time during transport via $\tau_{\rm mt} \approx \tau_{\rm st}/2$. Given the ranges for the total pulse time and distance, the mean velocity during transport lies between 1.75 m/s for a total protocol time of 0.01 ms to 5×10^{-3} m/s for a total time of 3 ms.

The hybrid ramps demonstrate a slight advantage when compared to the rest of the pulses, as they present a smaller effective temperature for total times $T \lesssim 1.5$ ms. Furthermore, the difference in the effective temperature among the hybrid ramps and the other pulses increases for shorter total times, reaching a difference of about 22 μK for $T \approx 0.3$ ms between the quadratic and the hybrid ramp with $\xi = 0.8$. Since the change of the energy after the evolution of a moving harmonic oscillator for a particle initially in one of the oscillator states is given by the Fourier transform of the acceleration evaluated at the frequency of the oscillator [1,56,68], a purely linear pulse does not induce heating during transport. The incorporation of the linear part in the hybrid trajectory presented in Ref. [10] uses the latter advantage and at the same time reduces the error after transport (as discussed on the basis of Fig. 3, the piecewise-linear pulse infidelity is more than 2 orders of magnitude higher when compared to the other pulses) induced by the velocity discontinuities at the endpoints of the pulse by replacing them with the minimum-jerk subintervals. In Appendix C, we report $\langle N \rangle$, ΔN, and $T_{\rm eff}$ as functions of time for total protocol times $T = 0.5$, 1.5, 2.5, and 3 ms. Here, it is possible to observe that for $T = 0.5$ ms, the hybrid pulse with $\xi = 0.8$ has the smaller ΔN and $T_{\rm eff}$, followed by the hybrid pulse with $\xi = 0.4$.

B. Atom-transport optimization

To further reduce the transport error, we implement an optimization protocol using the d-CRAB algorithm introduced by Rach *et al.* in 2015 [33–35,69]. This algorithm offers several advantages over other optimization methods, mainly because of its efficiency managing high-dimensional control spaces; by expanding the control pulses in a randomized basis, it reduces the dimensionality of the search space while circumventing local traps that could arise due to this restriction. Since within d-CRAB, only a small number of parameters are optimized at the same time, the need for gradient information is mitigated [70,71]. This makes it possible to perform adaptive optimal pulse shaping using experimental data, which implicitly allows experimental uncertainties—such as varying parameters and instrumentation transfer functions [72]—to be taken into account in the optimization cycle. We observe that, in practice, the flexibility offered by d-CRAB comes at the price of increased dependence on the initial guess for the controls; this is likely the result of a more local search in the control space. In light of this, the in-depth discussion of the relevant experimentally feasible pulses and the STA protocol that we presented in Sec. III becomes especially important.

We use the QuOCS library [32], which incorporates, among others, the d-CRAB algorithm in a user-friendly interface [35]. The QuOCS library allows for a straightforward setting of the parameters related to the pulse, such as the total time and basis parameters. It also allows the implementation of scaling functions that set appropriate limits on the position and amplitude control. We use an expansion of the control pulse in a basis of sigmoid functions and select only some of the coefficients as optimization control. We then conduct a systematic pulse optimization involving four different optimization schemes. Following the methodology outlined in Ref. [18], we optimize the trajectory for different total times and adjust the initial controls to identify the shortest achievable time during the numerical analysis.

The infidelity after transport as a function of the total time T for all the considered pulses is shown in Fig. 3 (bottom row). The optimization improves the fidelity by 2 orders of magnitude for the linear pulse and by one order of magnitude for the remaining pulses. For all the pulses, the shaded area corresponding to one standard deviation in the error over the last waiting interval of the pulse is reduced by the optimization, pointing toward a much more stable state after transport (see also Appendix C). The optimized piecewise-linear pulse reaches the infidelity value of 10^{-4} for a total time pulse of 55 $\tau_{\rm st}$. This threshold time remains at 18 $\tau_{\rm st}$ for the STA pulse, not changing appreciably after the optimization. The threshold time for the remaining pulses decreases between 10% and 30%; it changes from 48 $\tau_{\rm st}$ to 28 $\tau_{\rm st}$ for the hybrid pulse with $\xi = 0.8$, from 41 $\tau_{\rm st}$ to 28 $\tau_{\rm st}$ for the hybrid ramp with $\xi = 0.4$, from 32 $\tau_{\rm st}$ to 28 $\tau_{\rm st}$ for the minimum-jerk ramp, and from 38 $\tau_{\rm st}$ to 31 $\tau_{\rm st}$ for the quadratic pulse (all these times are indicated with dashed gray vertical lines). We conclude that the optimization yields a significant improvement for all the pulses; however, we would like to highlight that the full numerical solution for the STA protocol shows highly desirable features, even without optimization. In particular, our nonoptimized STA solution implies an improvement of 42% in the total time required to reach the fixed infidelity threshold of 10^{-4} with respect to the nonoptimized minimum-jerk pulse. In the case of the optimized ramps, the STA solution improves that time by 36% with respect to the optimized minimum-jerk pulse.

Since the objective of the optimization is to minimize the final infidelity, there is no guarantee that high-energy instantaneous eigenstates are not populated during the obtained transport dynamics, allowing the particle to escape the trap. For this reason, it is very important to check that the optimized pulses does not induce heating during the transport. As can be seen in Fig. 4 (bottom row), the optimization leads to higher vibrational excitations for the piecewise-linear and hybrid pulse with higher hybridization ($\xi = 0.8$). This feature is revealed when inspecting the effective temperature, but it is magnified by the behavior of the mean occupied level and the width of the distribution over the oscillator states, in line with the discussion presented in Ref. [64]. Our results suggest avoiding the use of piecewise-linear pulses, which are known to induce heating due to their intrinsic velocity discontinuities; this is consistent with the good fidelity obtained in Ref. [19] using a pulse with constant velocity in the central 10% of the transport interval ($\xi = 0.1$). The evolution of the infidelity, $\langle N\rangle$, ΔN, and $T_{\rm eff}$ is shown in Appendix C for total times $T = 0.5$, 1.5, 2.5, and 3 ms. Appendix C also contains a comparison between some examples of initial and optimized pulses. We would like to mention that a very small change in the pulse can translate into a considerable improvement of the fidelity, as was already exposed from the difference in the performance of the full numerical solution for the STA pulse when compared to the behavior of the approximated solution. Since all the optimized pulses except for the piecewise-linear one show limited heating, our results suggests that the use of d-CRAB for pulse shaping would not induce collateral heating that might cause major atom loss during transport.

As a final goal, we turn to the determination of good regions in the parameter space where the transport protocol can be reliably implemented in current experiments. We therefore focus on the two parameters that can be changed easily in the experiments, namely the total time of the pulse and the maximum amplitude (depth) of the moving tweezer. In fact, while the amplitude can be experimentally adjusted by manipulating the laser power, other parameters (such as the width of the tweezer) might be challenging to modify since they are ultimately determined by the optical elements within the apparatus. To identify good intervals for the amplitude and total time to run the experiments, in Fig. 5, we present heat maps for the optimized infidelity (minimizing the maximum of $\mathcal{I}$ over the last waiting interval) for the two pulses that enable reaching the infidelity threshold of 10^{-4} in the shortest total time for a fixed amplitude of $A_{\rm mt}^{\rm max}/\hbar = A_{\rm exp}/\hbar = 3.57 \times 2\pi$ MHz,

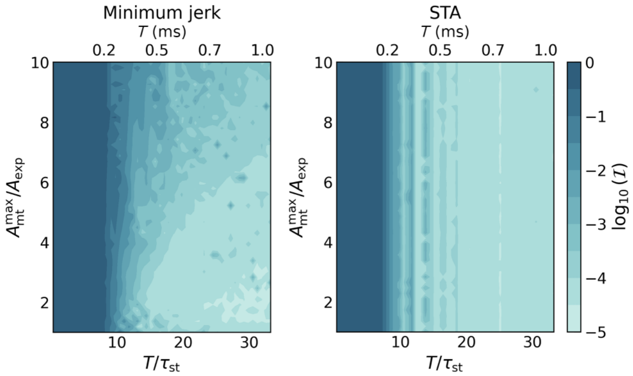

FIG. 5. Determining optimal regions in the experimentally accessible parameter space for high-fidelity transport pulses. The infidelity is shown for the minimum-jerk ramp (left) and our proposed STA pulse (right) after optimization as a function of the maximum amplitude $A_{\mathrm{mt}}^{\max}$. The amplitude is in units of $A_{\mathrm{exp}}/\hbar = 3.57 \times 2\pi$ MHz, and the total time of the pulse T is given in units of the characteristic time of the static traps τ_{st} (bottom scale) and in milliseconds (upper scale). Lighter colors show regions of smaller infidelity, which quantifies the error after transport. As before, the characteristic time during transport is given by $\tau_{\mathrm{mt}} \approx \tau_{\mathrm{st}}/2$ and the mean velocity during transport varies between 1.75 m/s for a total protocol time of 0.01 ms to 5×10^{-3} m/s for a total time of 3 ms.

i.e., the optimized minimum-jerk and STA pulses. We consider total times up to 1 ms $\sim 33\,\tau_{\mathrm{st}}$ (for larger total times, the infidelity reaches the stable regime) and maximum amplitudes between A_{exp} and $10\,A_{\mathrm{exp}}$, both being realistic ranges of the parameters for experimental realizations.

Our simulations show that the infidelity of the minimum-jerk pulse has a strong dependence on both the total time and the maximum amplitude. For larger amplitude values, longer times are needed to achieve a desired fixed value of the infidelity. We interpret this on the basis of the relation between the capturing and releasing time and the total time of the transport, which are here fixed to $T/5$ and $2\,T/5$ respectively. A higher amplitude of the moving tweezer implies a larger difference between the moving and static potential, meaning that the system requires a longer releasing time to adjust toward the target state. Fixing an error threshold of 10^{-4}, the best region in the parameter space appears for times longer than $20\,\tau_{\mathrm{st}}$ and amplitudes between 1 and $4\,A_{\mathrm{exp}}$. On the other hand, by incorporating a modulation in the amplitude of the moving tweezer that counteracts the restoring force of the static traps, the STA pulse depicts a quite robust infidelity against amplitude variations. Using our STA pulse, infidelities below 10^{-4} can be obtained for times longer than $20\,\tau_{\mathrm{st}}$ independently of $A_{\mathrm{mt}}^{\max}$. The STA ramps also seem to present *magic time windows*, exposed as lighter vertical stripes, indicating that the infidelity is suppressed by at least one order of magnitude around $T \approx 10.5\,\tau_{\mathrm{st}}$, $13.5\,\tau_{\mathrm{st}}$, $15.5\,\tau_{\mathrm{st}}$, $17.5\,\tau_{\mathrm{st}}$, and $25\,\tau_{\mathrm{st}}$. Such magic times have already been found in previous works addressing efficient atom transport. See for instance Refs. [25,31], where the authors combine reverse-engineering methods with quantum optimal control and design trajectories that show a strong suppression of the population across excited states for a given set of magic times [73].

Figure 5 shows a drastic increase in the infidelity for total pulse durations below $8\,\tau_{\mathrm{st}}$. This feature can already be inferred from Fig. 3 for all the considered pulses and for $A_{\mathrm{mt}}^{\max} = A_{\mathrm{exp}}$. Our results strongly point toward the presence of a QSL, imposing a bound for the minimum time required for the transport task [22,37]. Taking into account that the transport takes 2/5 of the total time, T, the bound for the transport time is about $3\,\tau_{\mathrm{st}}$. When comparing with the results for a quadratic pulse presented in Ref. [20] for the same setting (with a distance in oscillator units and a trap depth hosting the same amount of states) we observe that our lower bound for the transport time is five times larger; however, it is important to highlight that our protocol incorporates more information-processing details than the one considered in Ref. [20], where only the transport stage is taken into account with no consideration of the time devoted to capture and release the atom. For a moving trap hosting the same number of levels, we obtain a lower time threshold for the transfer between tweezers, which is nine times faster than the time reported in Ref. [19] (eight oscillator units versus 75 oscillator units). Considering that in Ref. [17], the authors state that the time needed for the capturing or releasing is 12 times that required for the transport task, our results suggests that an improvement of the transfer between tweezers can translate into an overall speedup, even at the cost of devoting a larger time to the transport stage. Our findings call attention to the importance of including the transfer between tweezers in the model; by optimizing over the entire process, which also includes the effect of the static traps, we see the importance of tailored solutions, such as those based on our specialized STA, for reaching error rates in the fault-tolerant regime.

V. SUMMARY AND CONCLUSIONS

In this work, we focused on the transport and transfer between tweezers of neutral atoms, a relevant problem (and possibly a bottleneck) for the creation and improvement of quantum processors and simulators [1,8]. We considered four different types of experimentally motivated pulses: piecewise-linear, piecewise-quadratic, minimum-jerk, and a family of hybrid linear and minimum-jerk ramps. These pulses were used to transport not only atomic ensembles but also few and single atoms in experiments with optical tweezers [1,7,8,10–12,17] and optical conveyor belts [48]. To generate a pulse that is specifically tailored for our problem, we developed a transport protocol using STA techniques. The main difference between our STA approach and previous ones is that we take into account the potential of the static tweezers to optimize the transfer between static and moving traps. To facilitate the adoption of our pulse in future experiments, we provided an easy-to-implement approximation for the full numerical solution. A close inspection of the approximated STA solution shows that the associated trajectory is a modification of the widely known minimum-jerk trajectory, with the key difference that its amplitude modulation (related to the depth of the moving trap) counteracts the effect of the static tweezers. We characterized the performance of all the considered pulses and found that our proposed STA protocol outperforms the experimentally inspired ramps, even without optimization.

All the considered pulses were used as initial guesses for QuOCS optimization, leading to a reduction in the error (quantified by the infidelity with respect to the target state) by at least one order of magnitude. By setting a threshold for the infidelity of 10^{-4}, we obtained a reduction of the total time of the pulse between 10% and 30% after optimization for the hybrid, minimum-jerk, and quadratic pulses.

Based on the discussions on heating and losses presented in Refs. [1,65], and to check that our optimized pulses do not induce extra heating during transport, we calculated the mean occupied level and the width of the distribution over the states of the moving tweezer, together with an effective temperature related to the motional energy. For total pulse times below $8\,\tau_{\mathrm{st}} \approx 16\,\tau_{\mathrm{mt}}$ (with τ_{st} and τ_{mt} being the characteristic times of the static and moving traps, respectively), the increase in the vibrational excitations exceeds half of the states hosted by the moving trap. We focused on the two pulses with the best performance, namely the minimum-jerk and STA pulses, and we quantified the error after transport as a function of the total time of the pulse and the maximum depth of the moving tweezer (which are both experimentally accessible parameters). We identified good regions in the parameter space to reliably run the transport protocol. For total times larger than $10\,\tau_{\mathrm{st}}$, both pulses provide good performance (with an infidelity below 10^{-2}); however, the minimum-jerk ramp entails limitations on the maximum amplitude that can be selected, while our proposed STA pulse provides much more freedom. We conclude that our STA solution constitutes an improvement compared to the usual minimum-jerk trajectory.

Our findings also suggest the presence of a lower bound for the total time of the pulses; we obtain a numerical quantum speed limit for the complete protocol time of about $8\,\tau_{\mathrm{st}}$. Since the transport time is a fraction of the total duration of the protocol, this value corresponds to a bound of $3\,\tau_{\mathrm{st}}$ for the transport stage, which is around five times the value reported in Ref. [20] for a protocol that does not consider the transfer time required to capture and release the atom. Taking into account that the capturing or releasing time was estimated to be 12 times larger than the time needed for the transport process alone in the experiments of Ref. [17], and that our obtained transfer time is nine times faster than the one reported in Ref. [19], our results draw attention to the relevance of including the transfer between tweezers in the model. In other words, to fully capture the information protocol, it is necessary to consider not only the transport process but also the transfer between optical tweezers, which makes up a significant portion (if not the majority) of the error and the time budget.

Our analytical and numerical results show that small deformations in the pulses (for instance, less than 4% for the approximated STA amplitude when compared to the full numerical solution) can translate into a decrease in the error after transport by 2 orders of magnitude. We also contribute to filling a knowledge gap identified in Ref. [48] in the case of atomic transport by means of optical conveyor belts, namely, providing a systematic characterization of the effectiveness of different trajectories.

Our proposed STA pulse also demonstrates that a modulation of the depth of the tweezer (in contrast to the widely used piecewise-linear ramps) counteracts the effect of the static tweezers, producing smaller and more stable errors for shorter pulse durations. This adds extra controllability, similarly to amplitude and phase control in optical lattices [74]. To the best of our knowledge, our proposed amplitude modulation could be implemented in current experiments since, as mentioned in Ref. [8], amplitudes with a quadratic dependence on time are possible. The implementation of the modulation in the tweezer depth as a second control that corrects the effects of the static tweezers is particularly promising in light of the recent experimental implementation of an STA trajectory which has many common elements to ours [61], with the key difference of correcting the static-tweezer effects during the transfer process. Our results contribute to the generalization and improvement of previously known ramps for transporting neutral atoms in state-of-the-art quantum processors and quantum simulators based on tweezer arrays. Given the flexibility of our approach to accommodate different external potentials, we are currently working on its application to optical lattice platforms.

ACKNOWLEDGMENTS

We thank Thomas Reisser for technical support related to QuOCS. We thank Jan Reuter and Matteo Rizzi for discussions about numerical stability. We also thank Christian Groß, Philip Osterholz, Yu Hyun Lee, Peter Bojovic, and Titus Franz for valuable discussions about the experimental possibilities. We acknowledge funding from the German Federal Ministry of Education and Research through the funding program quantum technologies—from basic research to market under FermiQP Project No. 13N15891, under Horizon

Europe programme HORIZON-CL4-2022-QUANTUM-02-SGA via Project No. 101113690 (PASQuanS2.1) and under HORIZON-CL4-2021-DIGITALEMERGING-02-10 via Grant Agreement 101080085 QCFD, by the Deutsche Forschungsgemeinschaft (DFG, German Research Foundation) under Germany's Excellence Strategy—Cluster of Excellence Matter and Light for Quantum Computing (ML4Q) EXC 2004/1—390534, and from the Jülich Supercomputing Center through the JUWELS and JURECA cluster. E.C. was supported by JSPS KAKENHI Grant No. JP23K13035.

DATA AVAILABILITY

The data that support the findings of this article are openly available [75].

APPENDIX A: STA THEORY

For the convenience of the reader, we regroup and summarize here the well-known results from the theory of shortcuts to adiabaticity (STA), which are relevant in the derivation of the STA-based transport pulse in Sec. III B.

1. Dynamical invariants and STA

Shortcuts to adiabaticity are a collection of methods whose aim is to obtain a fast-forward version of the adiabatic time evolution of a system. We exploit a known dynamical invariant of the system to reverse engineer an STA pulse that realizes the desired dynamics. Let us start by considering a time-dependent Hamiltonian $H(t)$ and the solutions $|\psi(t)\rangle$ to the Schrödinger equation

$$i\hbar\frac{\partial}{\partial t}\left|\psi(t)\right\rangle = H(t)\left|\psi(t)\right\rangle . \tag{A1}$$

A dynamical invariant of $H(t)$ is a time-dependent operator $I(t)$ that satisfies the relation

$$\frac{dI}{dt} \equiv \frac{\partial I}{\partial t} + \frac{1}{i\hbar}[I,H] = 0, \tag{A2}$$

meaning that $(d/dt)\langle\psi(t)|I(t)|\psi(t)\rangle$. Provided that $I^\dagger = I$ is Hermitian, it is possible to write any solution of Eq. (A1) as a time-independent linear combination of eigenvectors $\left|\phi_n^{\mathrm{LR}}(t)\right\rangle$ of $I(t)$ [30], which we denote as dynamical modes

$$\left|\psi(t)\right\rangle = \sum_n c_n\left|\phi_n^{\mathrm{LR}}(t)\right\rangle, \quad \text{with}$$
$$I(t)\left|\phi_n^{\mathrm{LR}}(t)\right\rangle = \lambda_n\left|\phi_n^{\mathrm{LR}}(t)\right\rangle, \tag{A3}$$

and where we explicitly state that the eigenvalues λ_n of $I(t)$ do not depend on time. Additionally, in the case that $I(t)$ does not involve a differentiation in time, the dynamical modes can be explicitly constructed by means of a gauge transformation of the (generic) eigenvectors $|\phi_n(t)\rangle$ of $I(t)$ [30], featuring the so-called Lewis-Riesenfeld phases $\gamma_n(t)$:

$$\left|\phi_n^{\mathrm{LR}}(t)\right\rangle = e^{i\gamma_n(t)}\left|\phi_n(t)\right\rangle , \tag{A4}$$

$$\hbar\frac{d\gamma_n}{dt} = \left\langle\phi_n(t)\right| i\hbar\frac{\partial}{\partial t} - H(t)\left|\phi_n(t)\right\rangle . \tag{A5}$$

In addition to being a useful tool to solve the equation of motion [Eq. (A1)], these modes can be used to find the Hamiltonian operator that produces a certain prescribed time evolution by means of reverse engineering. The goal is to realize a time evolution that maps eigenstates of $H(t_{\mathrm{i}})$ to eigenstates of $H(t_{\mathrm{f}})$ in a given amount of time $T = t_{\mathrm{f}} - t_{\mathrm{i}}$ (the subscripts i and f denote, as usual, initial and final). One way to obtain this is to impose that every dynamical mode coincides (up to a phase factor) with an eigenstate of the Hamiltonian at $t = t_{\mathrm{i}}, t_{\mathrm{f}}$. This requires the dynamical invariant to commute with the Hamiltonian at the endpoints of the time evolution, leading to the following boundary conditions:

$$[I(t_{\mathrm{i}}), H(t_{\mathrm{i}})] = [I(t_{\mathrm{f}}), H(t_{\mathrm{f}})] = 0. \tag{A6}$$

These are just necessary conditions, but they allow us to effectively speed up the adiabatic transfer between ground states at $t = t_{\mathrm{i}}$ and $t = t_{\mathrm{f}}$ in concrete cases, such as for atom transport [15].

2. STA for atom transport

A general family of Hamiltonians that is useful for atom transport and manipulation with a known dynamical invariant is given by Ref. [58]:

$$H(t) = \frac{p^2}{2m} - F(t)x + \frac{m}{2}\omega^2(t)x^2 + \frac{V\left(\frac{x-\alpha(t)}{\rho(t)}\right)}{\rho^2(t)}. \tag{A7}$$

It is possible to verify that for any constant ω_0, the operator

$$I(t) = \frac{[\rho(p - m\dot{\alpha}) - m\dot{\rho}(x-\alpha)]^2}{2m} + \frac{m\omega_0^2}{2}\left(\frac{x-\alpha}{\rho}\right)^2 + V\left(\frac{x-\alpha}{\rho}\right) \tag{A8}$$

is an invariant for $H(t)$, meaning that it satisfies Eq. (A2) provided that the following auxiliary conditions are also verified:

$$\ddot{\alpha} + \omega^2(t)\alpha = \frac{F(t)}{m} \quad \text{and} \tag{A9}$$

$$\ddot{\rho} + \omega^2(t)\rho = \frac{\omega_0^2}{\rho^3}. \tag{A10}$$

As proven in Ref. [58], there is a unitary transformation $|\phi\rangle = U(t)\,|\psi\rangle$ such that the transformed dynamical invariant $J = UIU^\dagger$, expressed in the coordinate $\zeta = \rho^{-1}(x-\alpha)$, is time independent. We can then obtain the eigenstates of I by solving the stationary eigenvalue problem for J and then transforming back with $U^\dagger$:

$$J\,|\phi_n\rangle = \lambda_n\,|\phi_n\rangle, \quad \text{with } |\psi_n(t)\rangle = U^\dagger(t)\,|\phi_n\rangle, \tag{A11}$$

which, in the coordinate space, gives rise to [15,58]

$$\left[-\frac{\hbar^2}{2m}\frac{\partial^2}{\partial\zeta^2} + \frac{1}{2}m\omega_0^2\zeta^2 + V(\zeta)\right]\phi_n(\zeta) = \lambda_n\phi_n(\zeta), \tag{A12}$$

$$\psi_n(x,t) = \rho^{-\frac{1}{2}} e^{\frac{im}{\hbar}[\dot{\rho}x^2/2\rho + (\dot{\alpha}\rho - \alpha\dot{\rho})x/\rho]}\phi_n\left(\frac{x-\alpha}{\rho}\right). \tag{A13}$$

Finally, the Lewis-Riesenfeld phases are obtained as [30,58]

$$\gamma_n(t) = -\frac{1}{\hbar}\int_0^t dt'\left(\frac{\lambda_n}{\rho^2} + \frac{m(\dot{\alpha}\rho - \alpha\dot{\rho})^2}{2\rho^2}\right), \tag{A14}$$

and the boundary conditions from Eq. (A6), which are necessary for eigenstate transfer, become

$$\dot{\alpha}(t_\mathrm{i}) = \ddot{\alpha}(t_\mathrm{i}) = \dot{\alpha}(t_\mathrm{f}) = \ddot{\alpha}(t_\mathrm{f}) = 0, \tag{A15}$$

$$\dot{\rho}(t_\mathrm{i}) = \ddot{\rho}(t_\mathrm{i}) = \dot{\rho}(t_\mathrm{f}) = \ddot{\rho}(t_\mathrm{f}) = 0, \tag{A16}$$

justifying Eqs. (15) and (16) in the main text. By fixing $F(t) = m\omega^2(t)x_0(t)$ and $V(x) = 0$ in Eq. (A7), we obtain the time-dependent harmonic-oscillator Hamiltonian [15] from Eq. (10), while Eqs. (A9)–(A10) become Eqs. (13)–(14), respectively, of the main text.

APPENDIX B: TIME-EVOLUTION METHOD AND DISCRETIZATION-ERROR ANALYSIS

Numerical simulations inherently contain errors, particularly if an infinite space is approximated by a finite one, as in the discretization of quantum-optical systems. For this reason, we examine the stability of the time evolution and investigate the error due to the space and time discretization. This is a crucial step in validating our numerical implementation. To evaluate the numerical errors present in our implementation, we study the harmonic oscillator under static and time-dependent conditions (using the same frequency ω_{st} and mass m as in the main text).

1. Space-discretization error analysis

The well-known solutions of the harmonic-oscillator problem allow us to study the error introduced by the space discretization, constrained only by the machine precision. We first compare the wave-function amplitude computed via exact diagonalization and the corresponding exact solution involving the Hermite polynomials for different space-discretization steps Δx. The analysis offers an understanding of the error range in the considered interval for space discretization. Calculating the root-mean-square error, $\mathcal{E}$, between the two different computation methods and fitting the resulting data, we relate $\mathcal{E}$ to the discretization step Δx as $\mathcal{E} = a\Delta x^b/(1+c\Delta x)$, with $a = 0.46$, $b = 2.31$, and $c = 7.03$, allowing for a selection of Δx once the error threshold is fixed.

Taking into account the required computational time and discretization precision, we found that $\Delta x \sim 0.02$ μm $\approx 0.2 l_{\mathrm{st}} \approx 0.4 l_{\mathrm{mt}}$ (where l_{st} and l_{mt} are respectively the characteristic lengths of the static and moving trap during transport, i.e., with maximum tweezer depth) is sufficient to capture the wave-function details while maintaining a discretization-error threshold of approximately 10^{-5} and a computational time in the range of milliseconds.

2. Time-discretization error analysis

The time evolution is performed using the split-step Fourier method [76–80], as explained in detail in Ref. [55]. This method is particularly effective thanks to the Baker-Campbell-Hausdorff relation [81]

$$e^{iH\Delta t} \simeq e^{-iV\Delta t/2}e^{-iT\Delta t}e^{-iV\Delta t/2} + \mathcal{O}(\Delta t^3), \tag{B1}$$

and the fast Fourier transform (FFT) algorithm [82]. In Eq. (B1), T and V denote the kinetic and potential terms of the Hamiltonian. We have chosen to reduce the error by introducing a symmetric splitting, also known as Strang splitting, where the potential is applied for a half time step before and after the kinetic operator, obtaining an error of $\mathcal{O}(\Delta t^3)$ [76,80]. The Fourier transform is used in the intermediate steps to diagonalize the operators T and V in their respective bases, reducing each multiplication in Eq. (B1) to a scaling of $\mathcal{O}(N)$. This combination allows us to develop a straightforward algorithm to compute the evolution of the state $|\psi(t)\rangle$ from time t to time $t+\Delta t$ that can be summarized in the following steps:

$$\begin{aligned} e^{-iH\Delta t}\,|\psi(t,x)\rangle &\approx e^{-iV\Delta t/2}e^{-iT\Delta t}e^{-iV\Delta t/2}\,|\psi(t,x)\rangle \\ &\propto U_V(x)\mathcal{F}^{-1}\mathcal{F}U_T(x)\mathcal{F}^{-1}\mathcal{F}U_V(x)\,|\psi(t,x)\rangle \\ &\propto U_V(x)\mathcal{F}^{-1}U_T(p)\,|\psi(t,p)\rangle \\ &\propto U_V(x)\,\left|\psi''(t,x)\right\rangle \\ &\propto |\psi(t+\Delta t,x)\rangle\,. \end{aligned} \tag{B2}$$

We have used $U_V = e^{-iV\Delta t/2}$, $U_T = e^{-iT\Delta t}$, and $\mathcal{F}$ denotes the Fourier transform. Moreover, the method assumes that the wave function does not change significantly within each small time step Δt.

To study our system described by a Hamiltonian

$$H(t) = \frac{p^2}{2m} + V(x) + V(x,t), \tag{B3}$$

we need to recursively apply the previous algorithm to the discretized potential $V(x, t_n) = V_n$, where $n = 0, 1, \ldots, N_t$, with N_t being the total number of time steps, which in our computation for $T = 3$ ms was chosen to be 5000 (see below), leading to $\Delta t = 0.6\ \mu\text{s} \approx 0.02\,\tau_{\text{st}} \approx 0.06\,\tau_{\text{mt}}$.

The FFT, with a scaling of order $N \log(N)$, is the primary source of the high computational cost, and a large number of time steps can further slow down the computation. At first glance, the single-splitting method given by

$$e^{iH\Delta t} \simeq e^{iV\Delta t} e^{iT\Delta t} + \mathcal{O}(\Delta t^2) \tag{B4}$$

could reduce the computational time of the time evolution; however, it incurs the cost of introducing high-order oscillations for the intermediate steps. To quantify the error and the amplitude of the induced oscillations, we studied the time evolution of a static harmonic oscillator by analyzing the infidelity between the time-evolved state and the analytical one for each time step (we use a fixed grid of 5000 time steps). We expect a vanishing infidelity due to the static nature of the harmonic oscillator; however, oscillations are observed at all time steps except the initial and final ones. The infidelity for the single-splitting method oscillates around 1.7×10^{-4}, while the infidelity obtained with the Strang splitting oscillates around 2.2×10^{-7} with the same oscillation period of two times the characteristic time of the oscillator. Even though the Strang splitting method is 30% slower, it leads to an improvement of more than 2 orders of magnitude in the infidelity, which is crucial for us to obtain faithful results for infidelities under 10^{-4}.

The time discretization Δt was chosen by analyzing the splitting methods for different total numbers of time steps. After a careful quantification of the effects of the oscillations in the evolution method, we compute the infidelity between the numerical and analytical harmonic-oscillator solution as a function of Δt and chose a grid of 5000 points for the larger considered total time of 3 ms to reach infidelities below 10^{-7}. With this procedure, smaller times will keep the error bound. When varying either the total evolution time in the range $[0.01, 3]$ ms or the frequency of the oscillator in the interval $[\omega_{\text{st}}, 10\,\omega_{\text{st}}]$, the relation between the two methods (Strang splitting and single splitting) is consistent, even though the error increases for increasing total times and frequencies. Finally, we used the transport trajectory obtained for the harmonic oscillator within our STA approach and calculated the root-mean-square error between the numerically computed and analytical solutions. In the latter case, we observe that the error for the Strang splitting is one order of magnitude less than that obtained using the single-splitting approach. For the final simulations, the grid in space and time has been chosen to find a compromise between obtaining higher fidelities while spending a reasonable computational time. Given that the experimental measurable errors are around 10^{-2} to 10^{-3}, we choose these grids to reach an infidelity of the order of 10^{-7} for a moving harmonic oscillator.

APPENDIX C: TRANSPORT DYNAMICS

In this section, we present the time evolution of the quantities studied in Sec. IV for some particular values of the total duration T of the protocol. We have chosen $T = 0.5$, 1.5, 2.5, and 3 ms, which corresponds to $16.6\,\tau_{\text{st}}$, $49.8\,\tau_{\text{st}}$, $83\,\tau_{\text{st}}$, and $99.6\,\tau_{\text{st}}$, or $55.7\,\tau_{\text{mt}}$, $167.1\,\tau_{\text{mt}}$, $278.4\,\tau_{\text{mt}}$, and $334.1\,\tau_{\text{mt}}$. At this point, it is important to remember that τ_{st} and τ_{mt} are the characteristic times of the static and moving trap during transport (i.e., with maximum tweezer depth), which are related by $\tau_{\text{st}} \approx 2\,\tau_{\text{mt}}$.

In Fig. 6 we report the error after transport measured as the maximum of the infidelity with respect to the target state over the last waiting interval of the pulse [see Eqs. (8) and (9)] for the five families of pulses considered in the main text. The upper row shows the results without optimization, while the error during transport obtained for the optimized pulses is depicted in the lower row. The darker the color of the curve, the larger the total time T. The evolution of the infidelity depicts more or less the same behavior for all the pulses; the fidelity is very low until the atom reaches the target tweezer, and after that, the fidelity rapidly increases. During the waiting stage of the pulse, the value of the infidelity presents some oscillations that can be seen as the thick final part of each curve. To interpret these results, it is important to have in mind that the data are presented in logarithmic scale; therefore, even though the STA final evolution seems to be very noisy, the final variations are spread on a 10^{-6} scale. Furthermore, for the hybrid pulse with $\xi = 0.4$ and the minimum-jerk ramp, the final infidelity is higher for $T = 3$ ms than for $T = 2.5$ ms, which is consistent with the oscillations of the infidelity when plotted against T (see Fig. 3 in the main text). All the optimized pulses improve the fidelity by at least one order of magnitude.

Figure 7 shows the time evolution of the mean occupied level of the moving trap states $\langle N\rangle$ and its uncertainty ΔN given by the width of the distribution over the states of the moving tweezer during transport (upper row), as well as the motional effective temperature T_{eff} (lower row). Since the nonoptimized and optimized curves are very similar except for the linear pulse, the values for the initial (nonoptimized) ramps are shown as gray curves,

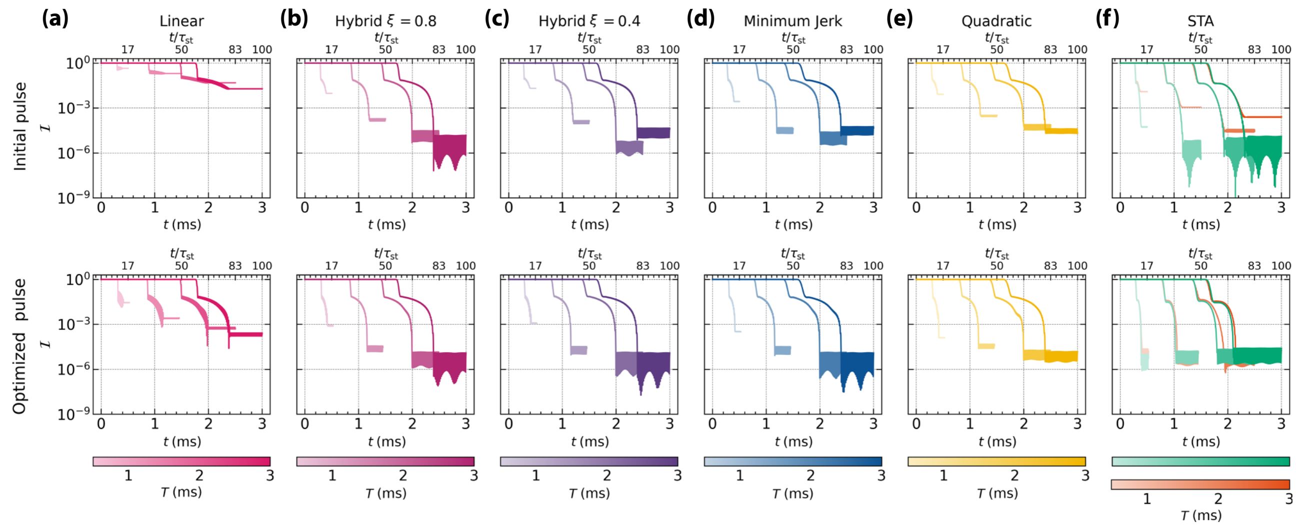

FIG. 6. Error during transport. Infidelity $\mathcal{I}$ vs time for total pulse times $T = 0.5$, 1.5, 2.5, and 3 ms (lighter to darker colors) for all the considered initial pulses (top row) and the corresponding optimizations (bottom row). The time scales are given in SI units and characteristic units, where the characteristic time τ_{st} of the static traps is related to the one of the moving trap via $\tau_{\mathrm{st}} \approx 2\,\tau_{\mathrm{mt}}$. All the pulses have a maximum amplitude of $A_{\mathrm{mt}}^{\max}/\hbar = 3.57 \times 2\pi$ MHz, the transport time is given by $\eta\,T$ with $\eta = 2/5$, and the total distance between static tweezers is $d = 7\ \mu$m.

and the values obtained for the optimized pulses are in color. As before, darker colors indicate longer total times. Shorter pulse times are related to higher $\langle N\rangle$, ΔN, and T_{eff} values. Furthermore, the optimization induces heating mainly for the piecewise-linear ramp, the hybrid one with hybridicity $\xi = 0.8$ (closer to the linear pulse), and the STA approximation. We notice that the distribution over the moving-tweezer states is more sensitive as a heating measure for transient times than the effective temperature. The two peaks depicted by $\langle N\rangle$ and ΔN correspond to the mixing of states induced when the wave function abandons one of the tweezers and readjusts into the following one.

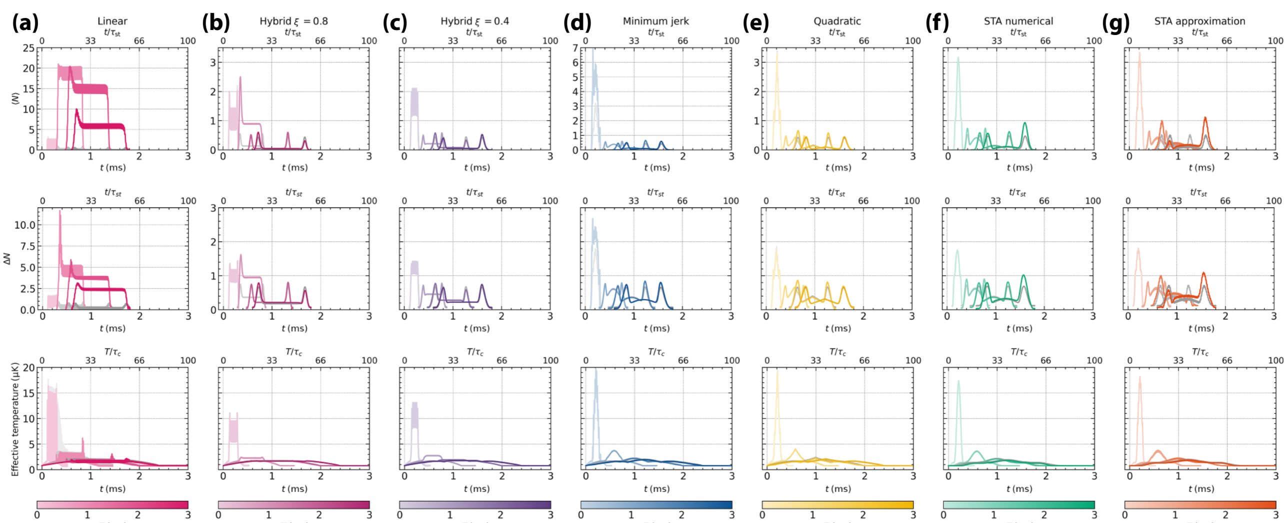

FIG. 7. Measures of heating during transport. Expected value $\langle N\rangle$ for the occupied level of the moving-trap states (top row) with the associated uncertainty ΔN (middle row), and effective temperature T_{eff} (bottom row) vs time for total pulse times $T = 0.5$, 1.5, 2.5, and 3 ms (lighter to darker colors) and for all the considered pulses. The colored curves correspond to the optimized pulses; the results obtained with the initial (nonoptimized) pulses are very similar (except for the piecewise-linear pulse) and are shown in gray behind each optimized curve. The time scales are given in SI units and characteristic units, with τ_{st} being the characteristic time of the static traps related to the one of the moving trap via $\tau_{\mathrm{st}} \approx 2\,\tau_{\mathrm{mt}}$. All the pulses have a maximum amplitude of $A_{\mathrm{mt}}^{\max}/\hbar = 3.57 \times 2\pi$ MHz, the transport time is given by $\eta\,T$ with $\eta = 2/5$, and the total distance between static tweezers is $d = 7\ \mu$m.

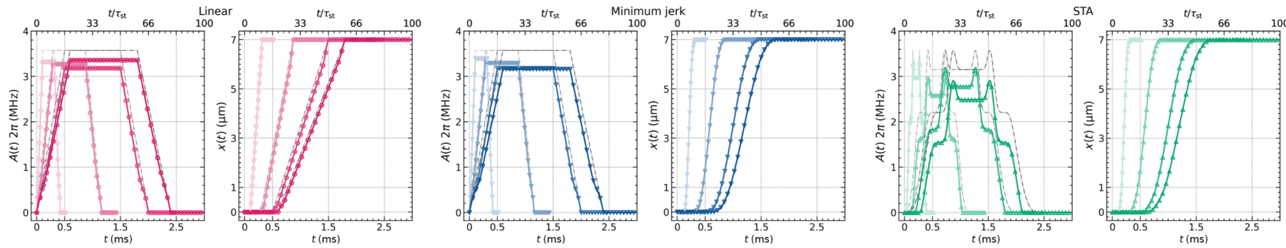

FIG. 8. Examples of optimized pulses. The amplitude $A_{\mathrm{mt}}(t)$ and the position $x_{\mathrm{mt}}(t)$ of the moving tweezer are shown for the linear (left), minimum-jerk (center), and STA (right) ramps. The optimized pulses are plotted in colored solid curves while the initial (nonoptimized) ones are depicted as gray dashed lines. We observe that the optimization results in small changes in the minimum-jerk and STA trajectories compared to the rest of the pulses. As before, the time scales are given in SI units and characteristic units, with τ_{st} being the characteristic time of the static traps related to the one of the moving tweezer via $\tau_{\mathrm{st}} \approx 2\,\tau_{\mathrm{mt}}$. All the pulses have a maximum amplitude of $A_{\mathrm{mt}}^{\max}/\hbar = 3.57 \times 2\pi$ MHz, the transport time is given by $\eta\, T$ with $\eta = 2/5$, and the total distance between static tweezers is $d = 7$ μm.

As expected due to the jumps in the velocity, in general, the piecewise-linear ramp depicts the highest $\langle N \rangle$ and ΔN values.

Finally, Fig. 8 presents examples of comparisons between the optimized pulses (colored solid lines) and the initial guesses or nonoptimized pulses (gray dashed lines) for the same total times, $T = 0.5$, 1.5, 2.5, and 3 ms, as considered before. We would like to highlight that the optimized position pulse for the linear ramp is not symmetric. This can also be seen in the asymmetric form depicted by $\langle N \rangle$ and ΔN in Fig. 7. While all the considered initial pulses were taken as symmetric, the automatic optimization algorithm breaks this symmetry, particularly for the piecewise-linear and approximated STA pulses. Furthermore, we observe that the optimization changes the piecewise-linear pulse mainly at the beginning and end of the transport stage; also, for the STA pulse, the optimization tends toward smaller amplitudes.

APPENDIX D: TRANSPORT AND TRANSFER ACROSS DIFFERENT DISTANCES AND VELOCITIES

The transport distance can range from a few micrometers to several hundreds of micrometers, depending on whether the transport occurs within the computational zone or between the storage and computational zones. We analyzed here the behavior of the minimum-jerk trajectory and the full numerical solution of our proposed STA pulse over distances between 1 and 14 μm. By way of example, in Fig. 9(a), we report the error after transport quantified by the infidelity $\mathcal{I}$ with the target state for a total distance of

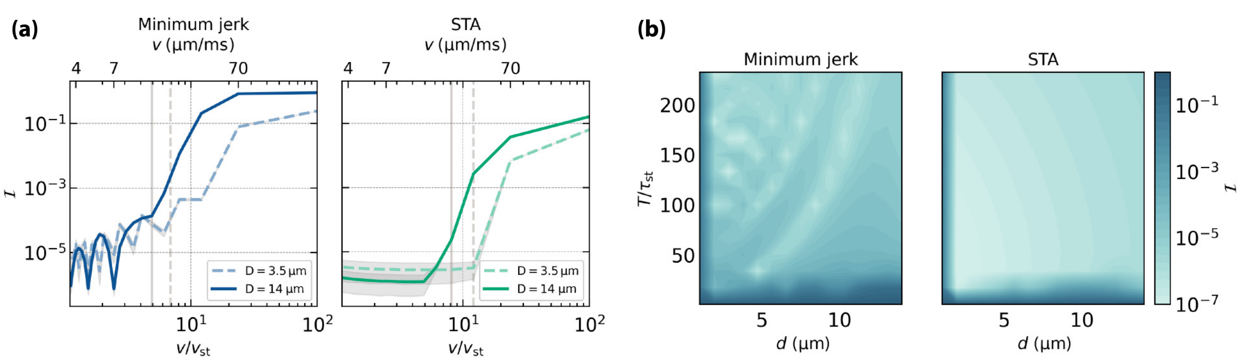

FIG. 9. Error during transport for larger distances. (a) Infidelity $\mathcal{I}$ vs velocity v in units of the characteristic velocity of the static oscillator v_{st} for distances of 3.5 and 14 μm (lighter-colored dashed line and darker-colored full line, respectively). The plots show the average infidelity over the last interval of the pulse (see Fig. 2) with the associated standard deviation (shaded area). The STA shows more stable behavior for both distances, followed by a speed up to reach the threshold infidelity of 10^{-4}; in particular, for a distance of 14 μm, that time reduces from $40\,\tau_{\mathrm{st}} \approx 1.21$ ms ($v = 0.014$ m/s) for the minimum jerk to $24\,\tau_{\mathrm{st}} \approx 0.75$ ms ($v = 0.024$ m/s) for the STA, while for a distance of 3.5 μm, it reduces from $32\,\tau_{\mathrm{st}} \approx 0.97$ ms ($v = 0.018$ m/s) to $16\,\tau_{\mathrm{st}} \approx 0.5$ ms ($v = 0.036$ m/s). (b) Infidelity $\mathcal{I}$ as function of the distance d and total time T. The time is varied between 0.01 and 7 ms, and the distance is ranges between 1 and 14 μm. For both pulses, the infidelity is higher at short times; however, while the minimum-jerk pulse shows a stronger dependence on T and d, the STA pulse exhibits much more stable behavior with lower infidelities.

3.5 μm and 14 μm (i.e., half and double the distance considered in the main text; transport over larger distances, although feasible, requires higher grid discretization and consequently longer computational times; for that reason, we stick to the typical range of distances found when moving atoms inside a determined zone and not among zones [17]), and a for total pulse time T ranging between 0.01 and 7 ms, corresponding to a mean velocity during transport varying between 1.75 and 0.0025 m/s. The figure shows the average infidelity over the last interval of the pulses and the associated standard deviation (shaded area) as a function of the mean velocity calculated as $d/(\eta T)$. Similar to what was observed for the original distance of 7 μm, the STA pulses depict a more stable behavior when compared to the minimum-jerk pulses. The infidelity increases as a function of the velocity. In both cases, the time needed for reaching the infidelity threshold of 10^{-4} increases with the distance. As before, the STA pulse allows for a reduction of approximately 40% in the time needed to obtain an infidelity of 10^{-4}.

In Fig. 9(b), we show the error $\mathcal{I}$ as function of both the distance d and the total time of the protocol T. The time ranges between 0.01 and 7 ms. while the distance is varied between 1 and 14 μm. For short distances and short total times, both protocols lead to errors above 10^{-1} due to the excitations induced by higher transport speeds. The bottom dark areas in the plots show the dependence of the quantum speed limit on the distance of the transport. Longer distances require a longer time; however, while the minimum jerk reaches infidelities of 10^{-6} or 10^{-7} in specific pairs of T and d, consistent with the oscillations present in Fig. 9(a), the STA shows a more stable and robust behavior on d and T. This suggest that the STA pulse not only reduces the error and the protocol time but it is also much more versatile than the considered experimentally inspired pulses.

[1] D. Bluvstein, H. Levine, G. Semeghini, T. T. Wang, S. Ebadi, M. Kalinowski, A. Keesling, N. Maskara, H. Pichler, M. Greiner, *et al.*, A quantum processor based on coherent transport of entangled atom arrays, Nature **604**, 451 (2022).

[2] A. Browaeys and T. Lahaye, Many-body physics with individually controlled Rydberg atoms, Nat. Phys. **16**, 132 (2020).

[3] A. J. Daley, I. Bloch, C. Kokail, S. Flannigan, N. Pearson, M. Troyer, and P. Zoller, Practical quantum advantage in quantum simulation, Nature **607**, 667 (2022).

[4] M. Morgado and S. Whitlock, Quantum simulation and computing with Rydberg-interacting qubits, AVS Quantum Sci. **3**, 023501 (2021).

[5] F. Gyger, M. Ammenwerth, R. Tao, H. Timme, S. Snigirev, I. Bloch, and J. Zeiher, Continuous operation of large-scale atom arrays in optical lattices, Phys. Rev. Res. **6**, 033104 (2024).

[6] D. Barredo, S. de Léséleuc, V. Lienhard, T. Lahaye, and A. Browaeys, An atom-by-atom assembler of defect-free arbitrary two-dimensional atomic arrays, Science **354**, 1021 (2016).

[7] M. Endres, H. Bernien, A. Keesling, H. Levine, E. R. Anschuetz, A. Krajenbrink, C. Senko, V. Vuletic, M. Greiner, and M. D. Lukin, Atom-by-atom assembly of defect-free one-dimensional cold atom arrays, Science **354**, 1024 (2016).

[8] D. Bluvstein, S. J. Evered, A. A. Geim, S. H. Li, H. Zhou, T. Manovitz, S. Ebadi, M. Cain, M. Kalinowski, D. Hangleiter, *et al.*, Logical quantum processor based on reconfigurable atom arrays, Nature **626**, 58 (2024).

[9] A. M. Kaufman and K.-K. Ni, Quantum science with optical tweezer arrays of ultracold atoms and molecules, Nat. Phys. **17**, 1324 (2021).

[10] L. R. Liu, J. D. Hood, Y. Yu, J. T. Zhang, K. Wang, Y.-W. Lin, T. Rosenband, and K.-K. Ni, Molecular assembly of ground-state cooled single atoms, Phys. Rev. X **9**, 021039 (2019).

[11] L. R. B. Picard, G. E. Patenotte, A. J. Park, S. F. Gebretsadkan, and K.-K. Ni, Site-selective preparation and multistate readout of molecules in optical tweezers, PRX Quantum **5**, 020344 (2024).

[12] J. T. Zhang, L. R. B. Picard, W. B. Cairncross, K. Wang, Y. Yu, F. Fang, and K.-K. Ni, An optical tweezer array of ground-state polar molecules, Quantum Sci. Technol. **7**, 035006 (2022).

[13] J. Tindall, M. Fishman, E. M. Stoudenmire, and D. Sels, Efficient tensor network simulation of IBM's eagle kicked Ising experiment, PRX Quantum **5**, 010308 (2024).

[14] J. Beugnon, C. Tuchendler, H. Marion, A. Gaëtan, Y. Miroshnychenko, Y. R. P. Sortais, A. M. Lance, M. P. A. Jones, G. Messin, A. Browaeys, and P. Grangier, Two-dimensional transport and transfer of a single atomic qubit in optical tweezers, Nat. Phys. **3**, 696 (2007).

[15] E. Torrontegui, S. Ibáñez, X. Chen, A. Ruschhaupt, D. Guéry-Odelin, and J. G. Muga, Fast atomic transport without vibrational heating, Phys. Rev. A **83**, 013415 (2011).

[16] Y. Chew, T. Tomita, T. P. Mahesh, S. Sugawa, S. de Léséleuc, and K. Ohmori, Ultrafast energy exchange between two single Rydberg atoms on a nanosecond timescale, Nat. Photon. **16**, 724 (2022).

[17] K.-N. Schymik, V. Lienhard, D. Barredo, P. Scholl, H. Williams, A. Browaeys, and T. Lahaye, Enhanced atom-by-atom assembly of arbitrary tweezer arrays, Phys. Rev. A **102**, 063107 (2020).

[18] M. R. Lam, N. Peter, T. Groh, W. Alt, C. Robens, D. Meschede, A. Negretti, S. Montangero, T. Calarco, and A. Alberti, Demonstration of quantum brachistochrones between distant states of an atom, Phys. Rev. X **11**, 011035 (2021).

[19] S. Spence, R. V. Brooks, D. K. Ruttley, A. Guttridge, and S. L. Cornish, Preparation of ^{87}Rb and ^{133}Cs in the motional ground state of a single optical tweezer, New J. Phys. **24**, 103022 (2022).

[20] A. Pagano, D. Jaschke, W. Weiss, and S. Montangero, Optimal control transport of neutral atoms in optical tweezers at finite temperature, Phys. Rev. Res. **6**, 033282 (2024).

[21] D. M. Reich, M. Ndong, and C. P. Koch, Monotonically convergent optimization in quantum control using Krotov's method, J. Chem. Phys. **136**, 104103 (2012).
[22] T. Caneva, M. Murphy, T. Calarco, R. Fazio, S. Montangero, V. Giovannetti, and G. E. Santoro, Optimal control at the quantum speed limit, Phys. Rev. Lett. **103**, 240501 (2009).
[23] L. Van Damme, Z. Zhang, A. Devra, S. J. Glaser, and A. Alberti, Motion-insensitive time-optimal control of optical qubits, Quantum Sci. Technol. **10**, 035025 (2025).
[24] M. Dalgaard, F. Motzoi, J. H. M. Jensen, and J. Sherson, Hessian-based optimization of constrained quantum control, Phys. Rev. A **102**, 042612 (2020).
[25] Q. Zhang, X. Chen, and D. Guéry-Odelin, Fast and optimal transport of atoms with nonharmonic traps, Phys. Rev. A **92**, 043410 (2015).
[26] Even though there is no dissipative mechanism considered in our model, we adhere to the identification of vibrational excitations and heating. See, for instance, Refs. [63,64,83].
[27] D. Guéry-Odelin, A. Ruschhaupt, A. Kiely, E. Torrontegui, S. Martínez-Garaot, and J. G. Muga, Shortcuts to adiabaticity: Concepts, methods, and applications, Rev. Mod. Phys. **91**, 045001 (2019).
[28] L. Theis, F. Motzoi, S. Machnes, and F. Wilhelm, Counteracting systems of diabaticities using drag controls: The status after 10 years, Europhys. Lett. **123**, 60001 (2018).
[29] S. Deffner, C. Jarzynski, and A. del Campo, Classical and quantum shortcuts to adiabaticity for scale-invariant driving, Phys. Rev. X **4**, 021013 (2014).
[30] H. R. Lewis and W. B. Riesenfeld, An exact quantum theory of the time-dependent harmonic oscillator and of a charged particle in a time-dependent electromagnetic field, J. Math. Phys. **10**, 1458 (1969).
[31] X. Chen, E. Torrontegui, D. Stefanatos, J.-S. Li, and J. G. Muga, Optimal trajectories for efficient atomic transport without final excitation, Phys. Rev. A **84**, 043415 (2011).
[32] M. Rossignolo, T. Reisser, A. Marshall, P. Rembold, A. Pagano, P. J. Vetter, R. S. Said, M. M. Müller, F. Motzoi, T. Calarco, *et al.*, QuOCS: The quantum optimal control suite, Comput. Phys. Commun. **291**, 108782 (2023).
[33] M. M. Müller, R. S. Said, F. Jelezko, T. Calarco, and S. Montangero, One decade of quantum optimal control in the chopped random basis, Rep. Prog. Phys. **85**, 076001 (2022).
[34] T. Caneva, T. Calarco, and S. Montangero, Chopped random-basis quantum optimization, Phys. Rev. A **84**, 022326 (2011).
[35] N. Rach, M. M. Müller, T. Calarco, and S. Montangero, Dressing the chopped-random-basis optimization: A bandwidth-limited access to the trap-free landscape, Phys. Rev. A **92**, 062343 (2015).
[36] A. Omran, H. Levine, A. Keesling, G. Semeghini, T. T. Wang, S. Ebadi, H. Bernien, A. S. Zibrov, H. Pichler, S. Choi, *et al.*, Generation and manipulation of Schrödinger cat states in Rydberg atom arrays, Science **365**, 570 (2019).
[37] S. Deffner and S. Campbell, Quantum speed limits: From Heisenberg's uncertainty principle to optimal quantum control, J. Phys. A **50**, 453001 (2017).
[38] I. Bloch, Ultracold quantum gases in optical lattices, Nat. Phys. **1**, 23 (2005).
[39] B. Yang, H. Sun, C.-J. Huang, H.-Y. Wang, Y. Deng, H.-N. Dai, Z.-S. Yuan, and J.-W. Pan, Cooling and entangling ultracold atoms in optical lattices, Science **369**, 550 (2020).
[40] C. Gross and I. Bloch, Quantum simulations with ultracold atoms in optical lattices, Science **357**, 995 (2017).
[41] M. Saffman, T. G. Walker, and K. Mølmer, Quantum information with Rydberg atoms, Rev. Mod. Phys. **82**, 2313 (2010).
[42] T. Chalopin, P. Bojović, D. Bourgund, S. Wang, T. Franz, I. Bloch, and T. Hilker, Optical superlattice for engineering Hubbard couplings in quantum simulation, Phys. Rev. Lett. **134**, 053402 (2025).
[43] L.-M. Steinert, P. Osterholz, R. Eberhard, L. Festa, N. Lorenz, Z. Chen, A. Trautmann, and C. Gross, Spatially tunable spin interactions in neutral atom arrays, Phys. Rev. Lett. **130**, 243001 (2023).
[44] P. Osterholz, Freely configurable holographic trap arrays for the trapping of single atoms, Master thesis, Ludwig Maximilians Universität München, 2020.
[45] Parameters suggested by Christian Groß group.
[46] G. Pesce, P. H. Jones, O. M. Maragò, and G. Volpe, Optical tweezers: Theory and practice, Eur. Phys. J. Plus **135**, 949 (2020).
[47] D. S. Simon, *Gaussian Beams and Lasers* (Morgan and Claypool Publishers, San Rafael, CA, USA, 2016), Chap. 3, pp. 3–1 to 3–14. 2053–2571.
[48] A. Matthies, Optical Conveyor-Belt Transport of Cs and Rb Atoms, Durham theses, Durham University, 2023.
[49] N. Hogan, An organizing principle for a class of voluntary movements, J. Neurosci. **4**, 2745 (1984).
[50] R. Jáuregui, Nonperturbative and perturbative treatments of parametric heating in atom traps, Phys. Rev. A **64**, 053408 (2001).
[51] D. Guéry-Odelin, A. Ruschhaupt, A. Kiely, E. Torrontegui, S. Martínez-Garaot, and J. G. Muga, Shortcuts to adiabaticity: Concepts, methods, and applications, Rev. Mod. Phys. **91**, 045001 (2019).
[52] X. Chen, A. Ruschhaupt, S. Schmidt, A. del Campo, D. Guéry-Odelin, and J. G. Muga, Fast optimal frictionless atom cooling in harmonic traps: Shortcut to adiabaticity, Phys. Rev. Lett. **104**, 063002 (2010).
[53] G. Ness, C. Shkedrov, Y. Florshaim, and Y. Sagi, Realistic shortcuts to adiabaticity in optical transfer, New J. Phys. **20**, 095002 (2018).
[54] Q. Zhang, J. G. Muga, D. Guéry-Odelin, and X. Chen, Optimal shortcuts for atomic transport in anharmonic traps, J. Phys. B **49**, 125503 (2016).
[55] S. H. Hauck and V. M. Stojanović, Coherent atom transport via enhanced shortcuts to adiabaticity: Double-well optical lattice, Phys. Rev. Appl. **18**, 014016 (2022).
[56] D. Guéry-Odelin and J. G. Muga, Transport in a harmonic trap: Shortcuts to adiabaticity and robust protocols, Phys. Rev. A **90**, 063425 (2014).
[57] S. H. Hauck, G. Alber, and V. M. Stojanović, Single-atom transport in optical conveyor belts: Enhanced shortcuts-to-adiabaticity approach, Phys. Rev. A **104**, 053110 (2021).
[58] A. K. Dhara and S. V. Lawande, Feynman propagator for time-dependent Lagrangians possessing an invariant quadratic in momentum, J. Phys. A **17**, 2423 (1984).

[59] S. K. Singh and S. Mandal, The solutions of the generalized classical and quantum harmonic oscillators with time dependent mass, frequency, two-photon parameter and external force: The squeezing effects, Opt. Commun. **283**, 4685 (2010).

[60] A. D. Campo and M. G. Boshier, Shortcuts to adiabaticity in a time-dependent box, Sci. Rep. **2**, 648 (2012).

[61] S. Hwang, H. Hwang, K. Kim, A. Byun, K. Kim, S. Jeong, M. P. Soegianto, and J. Ahn, Fast and reliable atom transport by optical tweezers, Optica Quantum **3**, 64 (2025).

[62] By fulfilling the same initial and final boundary conditions as the minimum-jerk trajectory, our STA solution also prevents heating arising from the acceleration at the beginning and end of the movement; however, since any translation with a nonconstant velocity profile implies a nonconstant sweeping rate in the AOD, which was associated with resonant intensity modulations (see Refs. [10,12]), we anticipate that our proposed STA position pulse could also be susceptible to this kind of heating. This point requires further experimental tests, and we foresee two possibilities, one is to solve it by implementing a closed-loop control optimization, and the other is to create a new hybrid pulse following the strategy of Kang-Kuen Ni's group as presented in Ref. [10] (i.e., avoid the resonant intensity modulations by including a constant sweep AOD rate for intermediate times) by mixing the STA and linear pulses.

[63] T. A. Savard, K. M. O'Hara, and J. E. Thomas, Laser-noise-induced heating in far-off resonance optical traps, Phys. Rev. A **56**, R1095 (1997).

[64] C. W. Gardiner, J. Ye, H. C. Nagerl, and H. J. Kimble, Evaluation of heating effects on atoms trapped in an optical trap, Phys. Rev. A **61**, 045801 (2000).

[65] G. T. Hickman and M. Saffman, Speed, retention loss, and motional heating of atoms in an optical conveyor belt, Phys. Rev. A **101**, 063411 (2020).

[66] C. Cohen-Tannoudji, B. Diu, and F. Laloë, *Quantum Mechanics* (Wiley, New York, 1977), Vol. 1.

[67] The expected value and maximum width of the distribution over the moving-tweezer states are computed on the transport interval as follows. For each time t, we compute the states $|\phi_n(t)\rangle$ of the moving trap via diagonalization of the moving-tweezer Hamiltonian. Then, we project the evolved wave function $|\psi(t)\rangle$ over each of these states to calculate the weights or populations over each state $p_n = |\langle\phi_n(t)|\psi(t)\rangle|^2$. Once we have the population distribution $\{p_n\}$, we calculate the variance and mean value as usual. We perform the same calculation using a harmonic approximation of the moving trap, and we check the consistency of the results. The maximum effective temperature $\max(T_{\text{eff}})$ is calculated over the complete protocol duration.

[68] P. Carruthers and M. M. Nieto, Coherent states and the forced quantum oscillator, Am. J. Phys. **33**, 537 (1965).

[69] P. Doria, T. Calarco, and S. Montangero, Optimal control technique for many-body quantum dynamics, Phys. Rev. Lett. **106**, 190501 (2011).

[70] V. Bergholm, W. Wieczorek, T. Schulte-Herbrüggen, and M. Keyl, Optimal control of hybrid optomechanical systems for generating non-classical states of mechanical motion, Quantum Sci. Technol. **4**, 034001 (2019).

[71] N. Khaneja, T. Reiss, C. Kehlet, T. Schulte-Herbrüggen, and S. J. Glaser, Optimal control of coupled spin dynamics: Design of NMR pulse sequences by gradient ascent algorithms, J. Magn. Reson. **172**, 296 (2005).

[72] J. Singh, R. Zeier, T. Calarco, and F. Motzoi, Compensating for nonlinear distortions in controlled quantum systems, Phys. Rev. Appl. **19**, 064067 (2023).

[73] The perturbative approach proposed in Ref. [25] for anharmonic traps can be applied to a fourth-order Taylor expansion of our tweezer potential to obtain an analytical estimation of the magic times; however, we would like to highlight that these theoretical results require further experimental tests.

[74] B. Khani, S. T. Merkel, F. Motzoi, J. M. Gambetta, and F. K. Wilhelm, High-fidelity quantum gates in the presence of dispersion, Phys. Rev. A **85**, 022306 (2012).

[75] C. Cicali, M. Calzavara, E. Cuestas, T. Calarco, R. Zeier, and F. Motzoi, Dataset for "Fast neutral atom transport and transfer between optical tweezers", available at: https://doi.org/10.5281/zenodo.16572794 (2025).

[76] S. Montangero, E. Montangero, and Evenson, *Introduction to Tensor Network Methods* (Springer, Cham, Switzerland, 2018).

[77] C. Lubich, *From Quantum to Classical Molecular Dynamics: Reduced Models and Numerical Analysis* (European Mathematical Society, Zürich, 2008), Vol. 12.

[78] W. Bao, S. Jin, and P. A. Markowich, On time-splitting spectral approximations for the Schrödinger equation in the semiclassical regime, J. Comput. Phys. **175**, 487 (2002).

[79] R. L. Speth, W. H. Green, S. MacNamara, and G. Strang, Balanced splitting and rebalanced splitting, SIAM J. Numer. Anal. **51**, 3084 (2013).

[80] S. MacNamara and G. Strang, in *Splitting Methods in Communication, Imaging, Science, and Engineering*, edited by R. Glowinski, W. Yin, and Stanley J. Osher (Springer, Cham, Switzerland, 2016), pp. 95–114.

[81] C. Cohen-Tannoudji, B. Diu, and F. Laloë, *Quantum Mechanics, Volume 3: Fermions, Bosons, Photons, Correlations, and Entanglement* (John Wiley & Sons, Weinheim, Germany, 2019).

[82] M. Frigo and S. G. Johnson, The design and implementation of FFTW3, Proc. IEEE **93**, 216 (2005).

[83] M. E. Gehm, K. M. O'Hara, T. A. Savard, and J. E. Thomas, Dynamics of noise-induced heating in atom traps, Phys. Rev. A **58**, 3914 (1998).